The Astrophysical Journal, 926:63 (22pp), 2022 February 10 https://doi.org/10.3847/1538-4357/ac408e


# The CGM–GRB Study. II. Outflow–Galaxy Connection at $z \sim 2$–6

Pradip Gatkine[1,2,7], Sylvain Veilleux[2,3], Daniel Perley[4], Joseph Durbak[5], Simone Dichiara[2,6], S. Bradley Cenko[3,6], and Eleonora Troja[2,6]
[1] Division of Physics, Mathematics and Astronomy, California Institute of Technology, Pasadena, CA 91125, USA; pgatkine@caltech.edu
[2] Dept. of Astronomy, University of Maryland, College Park, MD 20742, USA
[3] Joint Space Science Institute, University of Maryland, College Park, MD 20742, USA
[4] Astrophysics Research Institute, Liverpool John Moores University, IC2, Liverpool Science Park, 146 Brownlow Hill, Liverpool, L3 5RF, UK
[5] Dept. of Physics, University of Maryland, College Park, MD 20742, USA
[6] Astrophysics Science Division, NASA Goddard Space Flight Center, 8800 Greenbelt Rd, Greenbelt, MD 20771, USA
*Received 2020 October 21; revised 2021 November 23; accepted 2021 November 30; published 2022 February 11*

## Abstract

We use a sample of 27 gamma-ray bursts (GRBs) at redshift $z = 2$–6 to probe the outflows in their respective host galaxies ($\log(M_*/M_\odot) \sim 9$–11) and search for possible relations between the outflow properties and those of the host galaxies, such as $M_*$, the star formation rate (SFR), and the specific SFR (sSFR). First, we consider three outflow properties: outflow column density ($N_{\rm out}$), maximum outflow velocity ($V_{\rm max}$), and normalized maximum velocity ($V_{\rm norm} = V_{\rm max}/V_{\rm circ,halo}$, where $V_{\rm circ,halo}$ is the halo circular velocity). We observe clear trends of $N_{\rm out}$ and $V_{\rm max}$ with increasing SFR in high-ion-traced outflows, with a stronger ($>3\sigma$) $V_{\rm max}$–SFR correlation. We find that the estimated mass outflow rate and momentum flux of the high-ion outflows scale with SFR and can be supported by the momentum imparted by star formation (supernovae and stellar winds). The kinematic correlations of high-ion-traced outflows with SFR are similar to those observed for star-forming galaxies at low redshifts. The correlations with SFR are weaker in low-ion outflows. This, along with the lower detection fraction in low-ion outflows, indicates that the outflow is primarily high-ion dominated. We also observe a strong ($>3\sigma$) trend of normalized velocity ($V_{\rm norm}$) decreasing with halo mass and increasing with sSFR, suggesting that outflows from low-mass halos and high-sSFR galaxies are most likely to escape and enrich the outer circumgalactic medium (CGM) and intergalactic medium with metals. By comparing the CGM–GRB stacks with those of starbursts at $z \sim 2$ and $z \sim 0.1$, we find that over a broad redshift range, the outflow strength strongly depends on the main-sequence offset at the respective redshifts, rather than simply the SFR.

*Unified Astronomy Thesaurus concepts:* Circumgalactic medium (1879); Galactic winds (572); High-redshift galaxies (734); Galaxies (573); Galaxy evolution (594); Star formation (1569); Gamma-ray bursts (629); Intergalactic medium (813)

## 1. Introduction

Galactic inflows and outflows shape the evolution of galaxies as well as enrich the circumgalactic medium (CGM) and intergalactic medium (IGM). The gas inflows fuel star formation, while stellar winds, supernova (SN) explosions, and active galactic nuclei (AGNs) inject energy and metal-enriched matter (as well as entrained cold gas) at large distances into the interstellar medium (ISM) and CGM (Veilleux et al. 2005, 2020; Benson 2010; Booth & Schaye 2013; Tumlinson et al. 2017; Rupke 2018). The recycling flows from the CGM bring back the metal-enriched gas to refuel the star formation (Christensen et al. 2016). At the same time, removal of cold gas from the ISM can quench the star formation activity. Thus, galactic outflows regulate stellar buildup, and are an important piece of the galactic feedback puzzle. AGN-driven outflows are thought to be the dominant feedback process in massive galaxies (Veilleux et al. 2005; Fabian 2012; Heckman & Best 2014; King & Pounds 2015; Nelson et al. 2019), whereas SN-driven outflows are thought to be more important in low-mass, star-forming galaxies (Sharma & Nath 2012).

SN-driven outflows at high redshift are important for the early enrichment of the CGM and IGM (Tumlinson et al. 2017; Veilleux et al. 2020). The low-mass, star-forming galaxies are of particular interest in this context, since their outflows are most likely to escape their shallower potential wells. The relationship between the outflows and their host galaxies in the early universe holds the key to tuning the models of galactic feedback and understanding the history of galaxy growth and cosmic metal enrichment.

Observations at high redshift ($z > 2$) using various techniques have shown the presence of ubiquitous outflows in star-forming galaxies. The prominent techniques include down-the-barrel absorption line studies (Frye et al. 2002; Shapley et al. 2003; Sugahara et al. 2017; Du et al. 2018; Rudie et al. 2019), outflows at larger radii using background quasar or galaxy sightlines (Steidel et al. 2010; Lehner et al. 2014; Turner et al. 2014; Rudie et al. 2019), quasar–quasar pairings (Hennawi et al. 2006; Prochaska et al. 2014), observing lensed galaxy spectra (Rigby et al. 2018), spatially resolved spectroscopy in optical or radio (Harrison et al. 2012; Swinbank et al. 2015; Nielsen et al. 2020; Pizzati et al. 2020), and gamma-ray burst (GRB) afterglow sightlines (Fox et al. 2008; Gatkine et al. 2019). Galactic as well as cosmological zoom-in simulations provide the framework to understand the outflow mechanisms (for instance, Hirschmann et al. 2013; Shen et al. 2013; Muratov et al. 2015; Nelson et al.

[7] NASA Hubble Fellow.

2019; Mitchell et al. 2020). The high-$z$ outflow–galaxy relation and its evolution with redshift has recently been studied in Sugahara et al. (2017, 2019).

However, the outflow–galaxy relation in low-mass galaxies in the early universe remains poorly understood due to observational challenges. Two key challenges are: determining the redshift of the galaxy (in case of background QSO/galaxy sightlines) and obtaining high-quality absorption spectra of these faint galaxies (for the down-the-barrel technique). Apart from this, reliably removing the continuum spectrum of the background object can be a challenge.

The use of GRB sightlines to probe the outflows and CGM of its host galaxy offers a promising solution to these problems. In Gatkine et al. (2019), we described this method in detail. The main idea here is to use the bright GRB afterglow to probe the kinematics/outflows in the CGM of its host galaxy. GRB hosts at $z > 2$ are typically low-mass galaxies ($\log(M_*/M_\odot) < 10.5$), which makes them ideally suited for exploring the low-mass outflows that are difficult to probe using other techniques. The key advantages include: (1) clear identification of the host galaxy redshift; (2) high signal-to-noise ratio (S/N) and high-resolution spectra due to the bright GRB afterglow; and (3) the featureless continuum of the GRB afterglow eliminates the problem of continuum subtraction.

In this paper, we use the CGM–GRB sample compiled in Gatkine et al. (2019) to explore the correlations between outflow and galaxy properties. The CGM–GRB sample consists of 27 GRBs at $z \sim 2$–6 with high-S/N (median S/N $\sim$ 10) and high-resolution ($\delta v < 50$ km s$^{-1}$) spectra. Multicomponent Voigt profiles were fit to the absorption spectra of various high- and low-ion species (including C IV, Si IV, Si II, Fe II, and O VI). The CGM kinematics of this sample were studied in Gatkine et al. (2019). In this paper, we report the observations of their host galaxies in the optical and near-IR to estimate their star formation rate (SFR) and stellar mass ($M_*$). These observations and their analyses are described in Section 2. We then discuss the techniques used for visualizing and inferring correlations in Section 3. The key correlations between outflow properties and galaxy properties such as $M_*$, SFR, specific star formation rate (sSFR = SFR/$M_*$), and halo mass are detailed in Section 4. Finally, the implications of our results are discussed in Section 5.

Throughout this paper, we use the following model of cosmology: $H_0 = 70$ km s$^{-1}$ Mpc$^{-1}$, $\Omega_M = 0.3$, $\Omega_\Lambda = 0.7$.

## 2. Observations and Methods

As described earlier, we measure the galaxy properties in the CGM–GRB sample. The sample is selected strictly on the criterion of the availability of a high-resolution ($\delta v < 50$ km s$^{-1}$) and high-S/N (S/N $> 5$) afterglow spectrum. No cuts are made to the sample based on galaxy properties. The redshift distribution of the sample is shown in the first panel of Figure 2.

### 2.1. Optical Photometry

We performed optical photometry of previously unpublished or unobserved GRB hosts in the CGM–GRB sample. We observed GRB hosts using the 4.3 m Lowell Discovery Telescope (LDT). We also obtained deep archival imaging of two GRB hosts using the FORS instrument on the Very Large Telescope, and one each using HST (Hubble Space Telescope) WFC3 (program ID 15644), the Kilo-Degree Survey (KiDS) (Kuijken et al. 2019), and the PanSTARSS survey (Flewelling et al. 2020). We consider a GRB host as detected if the offset of the potential host and the GRB location is within 1″. The probability of a chance alignment of a galaxy brighter than the typical depth in our observations ($i$-band $\sim$ 24.7 AB mag) within 1″ is approximately 0.01 (see Figure 6 in Beckwith et al. 2006). At $z \sim 3$, 1″ roughly corresponds to 7.5 kpc. From previous HST observations of other GRB host samples at (Bloom et al. 2002; Fruchter et al. 2006; Lyman et al. 2017), more than 90% of the GRBs occur within this offset from their host galaxies. All the GRBs are localized with a <0.″5 precision. The resulting magnitudes are further corrected for Milky Way Galactic extinction using the dust maps of Schlafly & Finkbeiner (2011) and the extinction law with $R_V = 3.1$ from Cardelli et al. (1989). The photometry results are presented in Table 1.

**Table 1**
Summary of New Observations

| GRB | $z$[a] | Tel./Instr. | Filter | AB Mag |
|---|---|---|---|---|
| 000926A[b] | 2.0377 | Spitzer/IRAC | 3.6 $\mu$m | $25.2 \pm 0.15$ |
| 021004[b] | 2.3281 | Spitzer/IRAC | 3.6 $\mu$m | $24.22 \pm 0.18$ |
| 071031[c] | 2.6912 | Spitzer/IRAC | 3.6 $\mu$m | >25.3 |
| 080310[c] | 2.4274 | Spitzer/IRAC | 3.6 $\mu$m | $23.74 \pm 0.24$ |
| 090926A | 2.106 | Spitzer/IRAC | 3.6 $\mu$m | 22.96 ± 0.05 |
| | | VLT/FOR2 | $R_{\rm Special}$ | 23.9 ± 0.1 |
| 111008A[c] | 4.989 | Spitzer/IRAC | 3.6 $\mu$m | 24.73 ± 0.3 |
| | | HST/WFC3 | F110W | 25.5 ± 0.07 |
| 120327A | 2.813 | LDT/LMI | SL-r | $24.9 \pm 0.2$ |
| 130606A | 5.911 | Spitzer/IRAC | 3.6 $\mu$m | $24.91 \pm 0.25$ |
| 130610A | 2.091 | Spitzer/IRAC | 3.6 $\mu$m | 23.46 ± 0.05 |
| | | LDT/LMI | SL-r | 23.7 ± 0.1 |
| 141028A | 2.333 | Spitzer/IRAC | 3.6 $\mu$m | >25.1 |
| | | LDT/LMI | SL-r | >25.8 |
| 141109A | 2.993 | Spitzer/IRAC | 3.6 $\mu$m | 23.4 ± 0.1 |
| | | LDT/LMI | SL-i | 24.1 |
| 151021A | 2.329 | Spitzer/IRAC | 3.6 $\mu$m | >25.7 |
| | | KiDSSurvey | SL-r | 24.4 ± 0.2 |
| 151027B | 4.0633 | Spitzer/IRAC | 3.6 $\mu$m | >22.66 $24.8 \pm 0.4$ |
| | | LDT/LMI | SL − r | >24.3 |
| | | | SL-i | |
| 160203A | 3.518 | Spitzer/IRAC | 3.6 $\mu$m | 21.74 ± 0.02 |
| | | PanSTARRS | PS1-i | >22.7 |
| 161023A | 2.709 | Spitzer/IRAC | 3.6 $\mu$m | >25.9 |
| | | VLT/FORS2 | $R_{\rm Special}$ | >25.7 |
| 170202A | 3.645 | LDT/LMI | SL-r | >25.4 |
| | | | SL-i | >23.4 |

**Notes.**
[a] Redshifts taken from Gatkine et al. (2019).
[b] Spitzer Prog ID 40599, PI: R. Chary.
[c] Spitzer Prog ID 80054, PI: E. Berger. All other Spitzer observations are taken from Spitzer Prog IDs 11116, 13104, and 90062; PI: D. Perley.

The LDT imaging was performed using the Large Monolithic Imager (LMI; Massey et al. 2013). The LMI data was detrended with a custom python-based pipeline (Toy et al. 2016). Individual fields were astrometrically aligned and coadded using `SCAMP` and `SWARP`, respectively. The aperture photometry of the coadded images was performed using `Sextractor` with an aperture radius of ∼1.″5, which is typical of the average seeing in our observations. The magnitudes were calibrated against the Sloan Digital Sky Survey (Alam et al. 2015) and GAIA catalogs (Evans et al. 2018). Conversion of GAIA magnitudes to Sloan magnitudes

was performed using the conversion tables provided in GAIA data release 2 (Brown et al. 2018).

The FORS data was flat-fielded using the ESO pipeline `ESOreflex` (Freudling et al. 2013), and was further aligned, coadded, and calibrated as described above. The PanSTARSS and KiDS surveys provide reduced, stacked, and zero-point calibrated images, which were used to determine the science magnitudes/upper limits. The HST photometry was performed using archived drizzled and calibrated images, and the AB magnitude was derived using the provided zero-point. A 1″ aperture was used for HST images given the diffraction-limited imaging.

### 2.2. Spitzer IRAC Photometry

We obtained deep archival imaging of GRB hosts using the Spitzer Infrared Array Camera (IRAC) channel 1 (3.6 $\mu$m). Out of a total of 27 GRB hosts, we present new Spitzer IRAC photometry of 14 hosts in this paper, and 11 were previously published as a part of the SHOALS survey (Perley et al. 2016). The remaining two GRBs remained unobserved at the end of Spitzer mission. The newly presented data have been collected as part of various previous programs, which are summarized in Table 1.

By analyzing the new data the same way as Perley et al. (2016), we ensure procedural consistency with the previously published data. The reduction and photometry method is described in detail in Perley et al. (2016). Here, we briefly summarize the key points. We acquired the Level-2 Post-Basic Calibrated Data from the Spitzer Legacy Archive. We use the default astrometry provided with the Level-2 products (with an accuracy of 0.″3). Due to the large point-spread function (PSF) of Spitzer IRAC (∼1.″8 at 3.6 $\mu$m), source confusion and flux contamination from neighboring sources is an important issue. We compare each IRAC image with deep ground-based optical images (as described in Section 2.1) to identify the primary source and any neighboring contaminants. We use the `galfit` tool (Peng et al. 2002) over several iterations to model the sources (using the PSF and PRF files provided in the Spitzer documentation),[8] and subtract the neighboring sources that may contaminate the host or sky background regions. The subtracted image is then used for performing aperture photometry.

We implemented the IRAC handbook recommendations for aperture photometry using a custom IDL wrapper around the `aper` procedure in the Astronomy User's Library[9] (see Perley et al. 2016 for details). For aperture photometry, we place a 1.″8 aperture on the host galaxy location (guided by deep optical imaging) and a sky annulus with an inner radius of 3.″6 and outer radius of 6″. The source aperture and sky annulus are marked in red and yellow, respectively, in Figure 1. In the case of optical detection and IR nondetection, we specify a 2$\sigma$ limit. However, in the case of optical as well as IR nondetection, we evaluate a 3$\sigma$ upper limit to account for the uncertainty (typically <1″) in the GRB host location.

### 2.3. Stellar Mass

We use the Spitzer IRAC 3.6 $\mu$m photometry to infer the stellar masses of the galaxies in our sample. At $z \sim 2$–6, Spitzer IRAC measures the rest-frame optical light (beyond the Balmer break) from long-lived stars in the host galaxies. Here we follow the methodology used in Perley et al. (2016) to derive the stellar masses. Spectral energy distribution (SED) fitting is a more accurate method to estimate $M_*$ (by breaking the degeneracy between age and extinction). However, this requires extensive, ultradeep optical observations of faint GRB hosts in multiple filters, which is resource-intensive. Instead, we use Spitzer single-band (3.6 $\mu$m) photometry, which can still provide a reasonable estimate of stellar mass, particularly for galaxies at $z > 2$.

We calculate the absolute magnitude at $\lambda_{\rm rest} = 3.6\,\mu{\rm m}/(1+z)$ as $M_{\rm AB} = m_{\rm AB,3.6\,\mu m} - {\rm DM} + 2.5\log(1+z)$, where DM is distance modulus. In Perley et al. (2016), a grid of model galaxy SEDs is constructed for an array of redshifts ($z \sim 0$–10) and each decade in $M_*$ ($10^8$–$10^{11}$ $M_\odot$) by summing Bruzual & Charlot (2003) galaxy SED templates (using the Chabrier 2003 initial mass function). The models also incorporate a modest dust attenuation to validate the single-band stellar mass conversion function against the more accurate SED-fit (optical + Spitzer multiband) stellar masses in the MODS (Kajisawa et al. 2009) and UltraVISTA samples (Caputi et al. 2015). We then evaluate the stellar mass by interpolating on the $M_*$, redshift, and AB magnitude grid (see Perley et al. 2016 for more details). While the single-band method suffers from uncertainties associated with various model assumptions, such as the initial mass function, dust extinction ($A_V$), and star formation history, this method is consistent with the masses obtained from SED fitting at the ∼0.3 dex level. Further, by using the same method throughout our sample, we ensure that the correlations derived here are on an equal footing. The $M_*$ of our GRB hosts are summarized in Table 2.

### 2.4. Dust Correction

The ultraviolet (UV) dust extinction of the host galaxies needs to be estimated to convert the absolute magnitudes into intrinsic rest-frame UV luminosities. Following Greiner et al. (2015), we perform the dust correction using empirical correlations of the spectral index of the UV continuum $\beta$ (where $f_\lambda = \lambda^\beta$), the rest-frame absolute UV magnitude at $\lambda_{\rm rest} = 1600$ Å ($M_{\rm UV}$), and the dust extinction at rest-frame 1600 Å ($A_{1600}$). Here we assume that GRB hosts at high redshift follow a power-law SED ($f_\lambda = \lambda^\beta$) in the UV (redward of Ly$\alpha$) and the same correlations as the extensive high-$z$ (2.5–6) star-forming galaxy sample of >4000 galaxies from the HST HUDF and CANDELS surveys studied in Bouwens et al. (2009, 2014). They derive the following empirical relation for star-forming galaxies at $\langle z \rangle = 3.8$:

$$\beta = -1.85 - 0.11(M_{\rm UV} + 19.5). \quad (1)$$

The uncertainties on the numerical coefficients here are small ($-1.85 \pm 0.06$ and $-0.11 \pm 0.01$). Then, we iteratively solve for $M_{\rm UV}$ and $\beta$. The typical $\beta$ for the high-$z$ star-forming sample in Bouwens et al. (2009, 2014) is $\beta \sim -2$. In Equation (1), this corresponds to $M_{\rm UV} = -18.1$. Hence, we use $\beta = -2$ for our weaker upper limits (where $M_{\rm UV,lim} > -18.1$), where the value of $\beta$ is more uncertain. For stronger upper limits (i.e., $M_{\rm UV,lim} < -18.1$), we use the $\beta$ corresponding to the limit. Finally, the $A_{1600}$ is evaluated using

[8] https://irsa.ipac.caltech.edu/data/Spitzer/docs/irac/calibrationfiles/psfprf/
[9] https://idlastro.gsfc.nasa.gov/

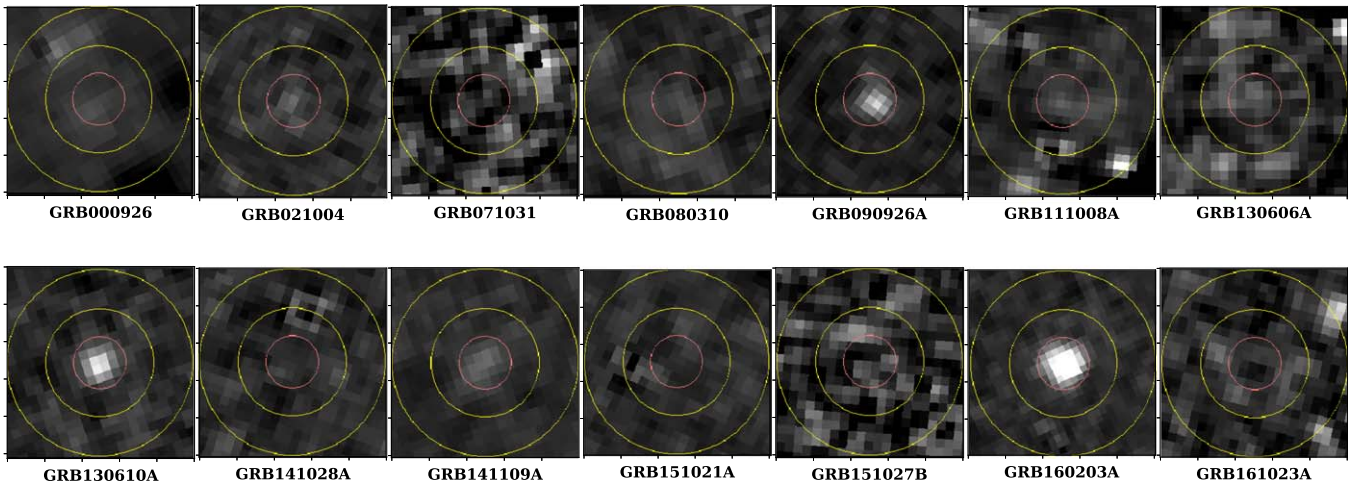


**Figure 1.** Contamination-subtracted images of GRB fields from Spitzer IRAC in the 3.6 $\mu$m band. Each thumbnail is $8'' \times 8''$ in size. The central red circle is the $1\farcs8$ aperture used to define the source flux, and the outer annulus is used to define the background flux. The circle is centered on the best-known position of the GRB or of the detected host galaxy. References for the GRB positions: 000926 (Fynbo et al. 2001), 021004 (Henden & Levine 2002), 071031 (Krühler et al. 2009), 080310 (Littlejohns et al. 2012), 111008A (Bolmer et al. 2018), 130606A (Castro-Tirado et al. 2013), 141109A (Xu et al. 2014), 151021A (McCauley & Melandri 2015), 151027B (Greiner et al. 2018), and 161023A (de Ugarte Postigo et al. 2018).

**Table 2**
Summary of GRB Host Properties in the CGM–GRB Sample

| GRB | $z$ | $\log(N_{\rm H\,I})$[a] | $A_V$[b] | $M_{3.6/(1+z)}$ | $\log(M_*/M_\odot)$ | $M_{\rm UV}$ | SFR ($M_\odot$ yr$^{-1}$) | References |
|---|---|---|---|---|---|---|---|---|
| 000926 | 2.0385 | $21.3 \pm 0.25$ | 0.15 | $-19.6$ | $9.3 \pm 0.3$ | $-19.5$ | $4.0^{+1.3}_{1.0}$ | Castro et al. (2003); Chen et al. (2009) |
| 021004[c] | 2.3281 | $19.0 \pm 0.2$ | 0.2 | $-20.9$ | $9.5 \pm 0.1$ | $-21.4$ | $11.8^{+3.7}_{-2.8}$ | Fiore et al. (2005); Fynbo et al. (2005) |
| 050730 | 3.9672 | $2.1 \pm 0.1$ | 0.12 | $>-20.5$ | $<9.46$[d] | $-18.1$ | $0.8^{+0.2}_{-0.1}$ | D'Elia et al. (2007); Toy et al. (2016) |
| 050820A | 2.6137 | $21.1 \pm 0.1$ | 0.08[e] | $-20.42$ | $9.4 \pm 0.15$[e] | $-19.1$ | $2.4^{+1.3}_{-0.9}$ | Prochaska et al. (2007); Chen et al. (2009) |
| 050922C | 2.1996 | $21.55 \pm 0.1$ | 0.10 | $-19.6$ | $<9.0$[e] | $>-18.3$ | $<1.0$ | Prochaska et al. (2008); Covino et al. (2013) |
| 060607A | 3.0738 | $16.95 \pm 0.03$ | 0.08 | $>-20.52$ | $<9.4$[e] | $>-17.5$ | $<0.4$ | Prochaska et al. (2008); Schady et al. (2012) |
| 071031 | 2.6912 | $22.15 \pm 0.05$ | 0.14 | $>-20.1$ | $<9.2$ | – | $1.4^{+0.3}_{-0.3}$[f] | Fox et al. (2008); Li et al. (2018) |
| 080310[c] | 2.4274 | $18.7 \pm 0.1$ | 0.10 | $-21.3$ | $9.8 \pm 0.1$[e] | $-19.0$ | $2.4^{+1.4}_{-0.9}$ | Fox et al. (2008); Perley et al. (2009) |
| 080804 | 2.205 | $21.3 \pm 0.1$ | 0.17 | $-20.2$ | $9.3 \pm 0.15$[e] | ⋯ | $15.1^{+20}_{-7}$[f] | Fynbo et al. (2009); Toy et al. (2016) |
| 080810[c] | 3.351 | $17.5 \pm 0.15$ | 0.40 | $-22.15$ | $10.24 \pm 0.1$[e] | $-22.9$ | $173^{+45}_{-36}$ | Page et al. (2009); Wiseman et al. (2017) |
| 090926A | 2.106 | $21.73 \pm 0.07$ | $<0.04$ | $-21.9$ | $9.8 \pm 0.1$ | $-20.5$ | $11.6^{+3.7}_{-2.8}$ | D'Elia et al. (2010); Zafar et al. (2018) |
| 100219A | 4.665 | $21.13 \pm 0.12$ | 0.13 | $>-20.4$ | $<9.4$[e] | $-20.0$ | $6.7^{+5.5}_{-3.2}$ | Thöne et al. (2012); Toy et al. (2016) |
| 111008A | 4.989 | $22.3 \pm 0.06$ | 0.12 | $-20.9$ | $9.5 \pm 0.2$ | $-20.5$ | $12.3^{+3.5}_{-2.7}$ | Sparre et al. (2014); Zafar et al. (2018) |
| 120327A | 2.813 | $22.01 \pm 0.09$ | $<0.03$ | $-23.2$ | $10.8 \pm 0.1$ | $-21.2$ | $28.1^{+12.5}_{-8.7}$ | D'elia et al. (2014); Heintz et al. (2019) |
| 120815A | 2.358 | $21.95 \pm 0.1$ | $0.19 \pm 0.04$ | $>-21.2$ | $<9.7$[e] | ⋯ | $2.3^{+2}_{-1}$[f] | Krühler et al. (2015); Zafar et al. (2018) |
| 120909A | 3.929 | $21.20 \pm 0.10$ | $0.16 \pm 0.04$ | $>-20.2$ | $<9.5$[e] | $-20.8$ | $17.9^{+6.2}_{-4.6}$ | Cucchiara et al. (2015); Heintz et al. (2019) |
| 121024A[c] | 2.298 | $21.50 \pm 0.10$ | 0.56[e] | $-21.8$ | $10.15 \pm 0.15$ | $-21.7$ | $37^{+20}_{-15}$ | Friis et al. (2015); Toy et al. (2016) |
| 130408A | 3.757 | $21.70 \pm 0.10$ | 0.2 | ⋯ | ⋯ | $>-21.1$ | $<13.4$ | Zafar et al. (2018) |
| 130606A | 5.911 | $19.93 \pm 0.2$ | $<0.07$ | $-21.8$ | $10.0 \pm 0.2$ | $-19.9$ | $6.3^{+2.4}_{-1.7}$ | Hartoog et al. (2015); Zafar et al. (2018) |
| 130610A | 2.091 | ⋯ | 0.01 | $-21.3$ | $9.7 \pm 0.05$ | $-20.6$ | $13^{+4.1}_{-3.1}$ | Smette et al. (2013); Littlejohns et al. (2015) |
| 141028A | 2.333 | $20.60 \pm 0.15$ | 0.13 | $>-20.0$ | $<9.2$ | $>-19.2$ | $<2.3$ | Wiseman et al. (2017) |
| 141109A | 2.993 | $22.10 \pm 0.10$ | 0.11 | $-22.1$ | $10.1 \pm 0.1$ | $-20.9$ | $19.7^{+14}_{-8}$ | Heintz et al. (2018); Heintz et al. (2019) |
| 151021A | 2.329 | $22.3 \pm 0.2$ | 0.2 | $>-19.4$ | $<9.0$ | $-20.3$ | $9.6^{+4.3}_{-3}$ | Heintz et al. (2018) |
| 151027B | 4.0633 | $20.5 \pm 0.2$ | $<0.12$ | $-23.45$ | $<10.8$ | $-21.9$ | $58^{+40}_{-24}$ | Heintz et al. (2018); Zafar et al. (2018) |
| 160203A | 3.518 | $21.75 \pm 0.10$ | $<0.1$ | $-24.2$ | $11.2 \pm 0.05$ | $>-22.9$ | $<71$ | Heintz et al. (2018) |
| 161023A | 2.709 | $20.96 \pm 0.05$ | 0.09 | $>-19.5$ | $<9.1$ | $>-19.6$ | $<3.4$ | Heintz et al. (2018); de Ugarte Postigo et al. (2018) |
| 170202A | 3.645 | $21.55 \pm 0.10$ | $<0.12$ | ⋯ | ⋯ | $>-21.0$ | $<11.5$ | Selsing et al. (2019); Zafar et al. (2018) |

**Notes.** Column descriptions: $M_{3.6/(1+z)}$: AB magnitude in rest-frame optical/NIR from Spitzer data; $M_{\rm UV}$: Absolute magnitude at $\lambda_{\rm rest} = 1600$ Å; SFR: in units of $M_\odot$ yr$^{-1}$.

[a] Neutral hydrogen column densities (in cm$^{-2}$) measured from the damped Ly$\alpha$ absorption, unless noted otherwise.

[b] Extragalactic dust extinction in magnitude, derived assuming the SMC extinction law (Gordon et al. 2003).

[c] GRBs with deep VLA observations from Gatkine et al. (2020).

[d] Derived using the host galaxy SED.

[e] From Perley et al. (2016).

[f] 071031: SFR using Ly$\alpha$ Milvang-Jensen et al. (2012); 080804: SFR using H$\alpha$ Krühler et al. (2015); 120815: SFR using H$\alpha$ Krühler et al. (2015).

the following relation from Meurer et al. (1999):

$$A_{1600} = 4.43 \text{ mag} + 1.99\beta. \quad (2)$$

This dust correction method is described in detail in Greiner et al. (2015).

### 2.5. Star Formation Rate

We use single-band photometry in the rest-frame UV to calculate the UV-based SFR. To compute the SFR from the dust-corrected UV luminosity ($L_{\rm UV,corr}$), we follow the relations described in Savaglio et al. (2009), where they simultaneously compare the emission line and dust-corrected UV luminosities of GRB hosts to derive the conversion factor between the dust-corrected UV luminosity and SFR. We use the $A_{1600}$ and $M_{\rm UV}$ values calculated in Section 2.4 to compute $L_{\rm UV,corr}$. The SFR is then calculated as follows:

$$\text{SFR}_{1500} = 1.62\, M_\odot \text{ yr}^{-1} \times \frac{L_{1500,\rm corr}}{10^{40} \text{ erg s}^{-1} \text{ Å}^{-1}}. \quad (3)$$

As a validation step, we compare the $A_{1600}$ evaluated using the $\beta$ method with that using the afterglow-derived $A_V$ (assuming an SMC extinction law). The resulting SFRs derived using the two methods are consistent with each other within a factor of two, except for GRBs 130408A and 080810, where the afterglow $A_V$ is larger, leading to a higher SFR estimate (for the afterglow $A_V$ method) by a factor of three. Nonetheless, it is important to note that the afterglow-derived extinction corresponds to a single sightline, while the extinction derived using the $\beta$ method is an average value for the host. The SFRs of our GRB hosts are summarized in Table 2.

For GRBs 071031, 080804, and 120815, photometric observations are either unavailable or too shallow. In the case of GRBs 080804 and 120815, we have used H$\alpha$ emission line-based SFRs from Krühler et al. (2011), since they are more robust compared to UV luminosity. For GRB 071031, we use the Ly$\alpha$-based SFR from Milvang-Jensen et al. (2012). While less robust, this measurement is consistent with the upper limit of $3 M_\odot$ yr$^{-1}$ from an archival HST WFC3 (F160W filter) observation.

Note, however, that our sample naturally has low line-of-sight dust extinction compared to the general GRB host population, since we only select the afterglows that are bright enough for high-resolution rest-frame UV spectroscopy. While there may be a systematic bias in the dust correction, we have used the same SFR tracer and analysis procedure for the entire sample (except GRBs 071031, 080804, and 120815), thus minimizing any relative bias. Our sample may contain a small number of heavily dust-enshrouded galaxies, for which we may underestimate the SFR. However, we have minimized this possibility by ruling out heavy dust obscuration in four massive GRB hosts in our sample (where the probability of heavy dust obscuration is high) by using deep VLA observations (Gatkine et al. 2020), and hence the typical dust corrections described here can be used for estimating their SFRs. These GRBs are marked with asterisks in Table 2.

## 3. Sample Properties and Analysis

### 3.1. Comparison with Star Formation Main Sequence

Figure 2 shows the distribution of $M_*$, SFR, and $z$ of the CGM–GRB sample. We compare the relative position of our sample with respect to the star-forming main sequence at $z = 2$ and 4. The star-forming main sequence and its scatter is computed using Equation (28) in Speagle et al. (2014). The key characteristics of our sample in terms of galaxy properties are summarized below.

1. We divide the sample into two groups—$z1$: 2–2.7 and $z2$: 2.7–5.9—that have equal numbers of objects and roughly equal cosmological timescales (1 and 1.4 Gyr). We highlight that there is no significant difference in the two groups in terms of SFR distribution. On the other hand, the host galaxy stellar mass distribution of the high-$z$ group is biased toward higher masses, as shown in Figure 2 (panel 3). However, note that this is not an intrinsic bias in the sample selection, since our sample is selected based only on the afterglow properties. Regardless, from Figure 2, we conclude that our sample primarily traces the low-mass end of the galaxy mass function at the respective redshifts (by comparing against the characteristic stellar mass in the Schechter function).
2. While there is a significant spread, the majority of the GRB hosts in our sample are within 0.5 dex (i.e., 3×) of the star formation main sequence at their respective redshifts (within observational uncertainties). It should also be noted that the majority of the GRB hosts here are below the main sequence. Thus, our sample traces a moderately sub-main-sequence galaxy population at $z \sim 2$–6.

### 3.2. Blue-wing Column Density and Outflows

To quantify outflows, we use the multicomponent Voigt profile fits to the high-resolution GRB afterglow absorption spectra (in the rest-frame UV) and the resulting column densities from Gatkine et al. (2019). We then integrate the apparent column density (derived from the fit) blueward of $-100$ km s$^{-1}$. We define this quantity as the blue-wing column density ($N_{\rm out}$), which is a measure of the galactic outflow. This velocity threshold is carefully chosen to minimize any contamination from the line-of-sight absorption in the ISM. A detailed justification for this limit is provided in Gatkine et al. (2019) through kinematic and geometric modeling of the ISM + CGM of a representative galaxy in this sample (see Sections 3.1, 5, 7.4, and Appendix B in Gatkine et al. 2019). This is similar to down-the-barrel observations of outflows, albeit with random sightlines and using high-resolution and high-S/N spectra.

We compare the blue-wing column density as described above with the host galaxy properties ($M_*$ and SFR). In particular, we focus on four species. These include two high-ionization potential species (high-ion)—C IV and Si IV—and two low-ionization potential species (low-ion)—Si II and Fe II. Primarily, we used C IV 1550, Si IV 1402, Si II 1526, and Fe II 1608 absorption lines to trace the outflow–galaxy relations (summarized in Figures 3–10). These species are selected for three reasons. (1) Their absorption lines fall within the passbands over a large redshift range at $z > 2$. (2) These lines are not too weak (leading to underestimates) or not too strong (saturated). In most cases, we do not have saturation in the blue wings. (3) They allow us to compare the differences between the relations of high-ion and low-ion species with host galaxy properties.

In particular, for low-ion lines, other alternatives have been used in the literature, including Si II 1260, O I 1302, and C II 1334. However, we did not use them as the primary focus of

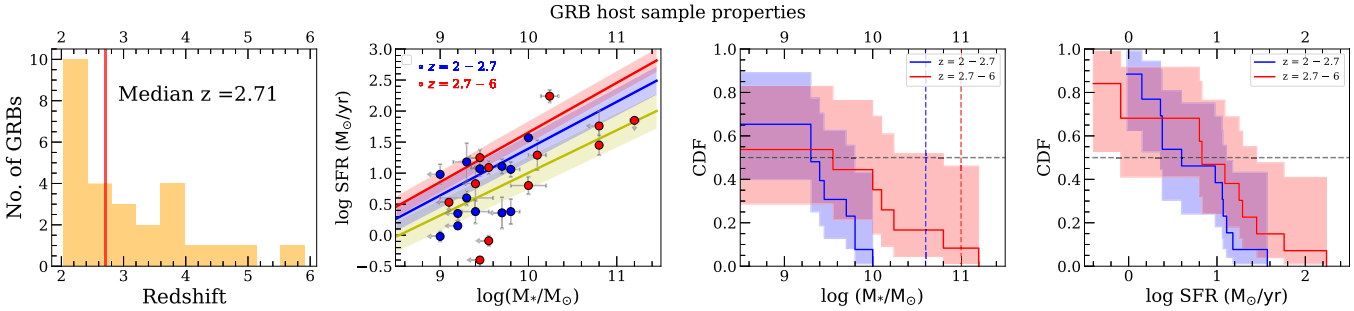


**Figure 2.** Properties of the CGM–GRB sample. Panel 1: the redshift distribution of the sample. Panel 2: the SFR vs. $M_*$ of the GRB host galaxies in our sample. The lines show the main-sequence curves (yellow: $z = 1$; blue: $z = 2$; red: $z = 4$) as described in Speagle et al. (2014). Panel 3: the cumulative distribution of the stellar mass in the CGM–GRB sample. The spread shows a 95% confidence interval around the value by incorporating any upper limits. The dotted vertical lines show the value of characteristic mass, $M^*$ in the mass function (written as a Schechter function), at the respective redshifts. The horizontal line shows the median (i.e., CDF = 0.5). Panel 4: the same as panel 3, for SFR.

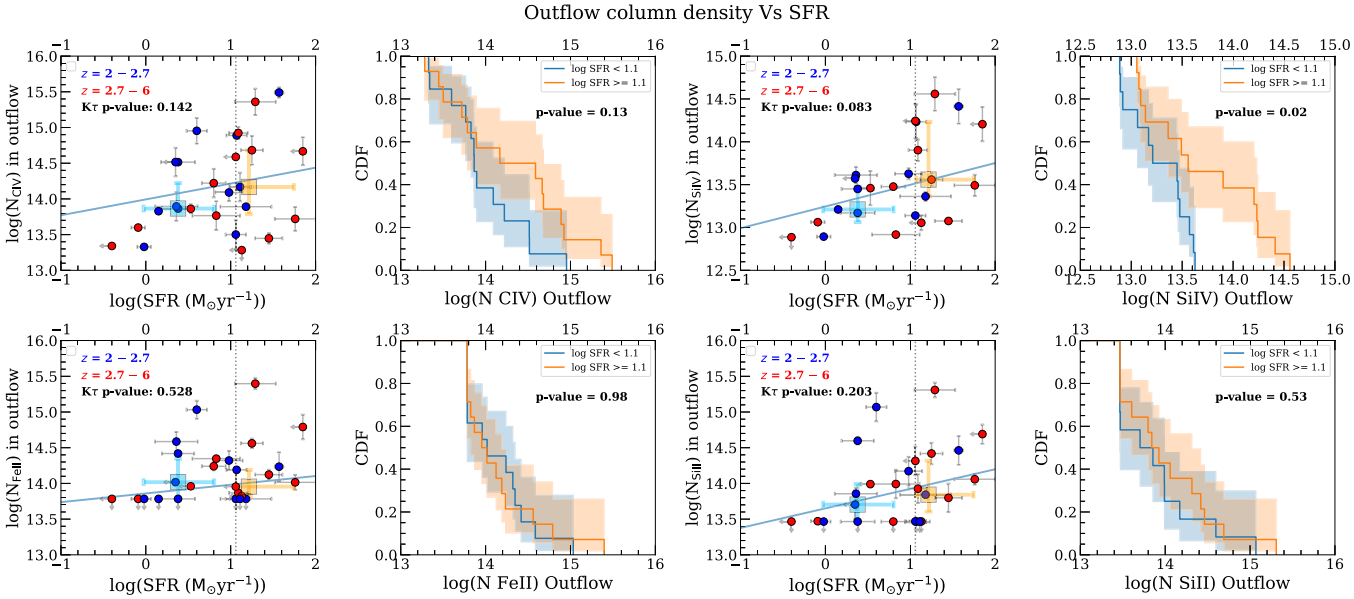


**Figure 3.** Column density in the outflows in GRB hosts traced by high-ion (C IV, Si IV) and low-ion (Fe II, Si II) species vs. their SFR. The Kendall-$\tau$ $p$-value indicates the strength of correlation ($1 - p$ is the confidence level of the correlation). The vertical dotted line splits the sample into two equal groups around the median SFR. The CDF of each group is shown on the right to compare the distributions of the low-SFR and high-SFR parts of the sample. The log-rank test $p$-value shown in the CDF plot measures the extent to which the distributions are similar and hence consistent with no correlation. The median and 68-percentile spread of the median column density is shown using the blue and orange squares. The best-fit line (including limits in the data) is also shown here. Apart from a weak correlation, there is a significant increase in the spread of column density at high SFR (particularly for the high-ion lines).

the correlation investigation to avoid potential blending issues. Notably, Si II 1260 has the most severe blending issue, due to S II 1259, which is essentially at a velocity offset of $-200$ km s$^{-1}$. This can be seen in Figure 11, showing the stacks of the respective lines in the CGM–GRB sample. Therefore, it is difficult to reliably integrate Si II 1260 for measuring the outflows. For C II 1334 and O I 1302, the blending issues (due to C II$^*$ 1335 and Si II 1304, respectively) are less severe for the outflows. Hence, we used Si II 1526 and Fe II 1608, which are free from such blending issues, for the primary investigation of the correlations. We further conducted a secondary investigation with O I 1302 and C II 1334 as a consistency check. Those results are summarized in Appendix C.

### 3.3. Inferring Correlations and Hypothesis Testing

To investigate the presence of correlations between outflow and galaxy properties, we primarily focus on the parameter space of logarithms of $M_*$, SFR, outflow column density, and maximum outflow velocity. First, we perform a Kendall-$\tau$ test by using the null hypothesis that there is no intrinsic correlation between the two parameters. The $1 - p$-value from the Kendall-$\tau$ test gives us the confidence level at which the null hypothesis is rejected (i.e., a smaller $p$-value implies the higher probability of the existence of a correlation). Second, we perform a linear regression to infer the best-fit line for each investigated correlation, using Schmitt's binned regression (Schmitt 1985). Note that we include all the upper (and lower) limits in both of these analyses, using the astronomy survival analysis code called ASURV (Feigelson & Nelson 1985; Isobe et al. 1986; Isobe & Feigelson 1990). The resulting best-fit and Kendall-$\tau$ $p$-values are shown in the correlation figures.

Due to multiple upper limits in the stellar masses and/or SFRs in the sample, simply using linear regression does not provide complete information about the underlying correlations and/or their spread. Therefore, we also divide the sample into two equal parts (around the median) based on the galaxy property under consideration ($M_*$ or SFR), and investigate whether the sample distributions of the outflow property (e.g.,

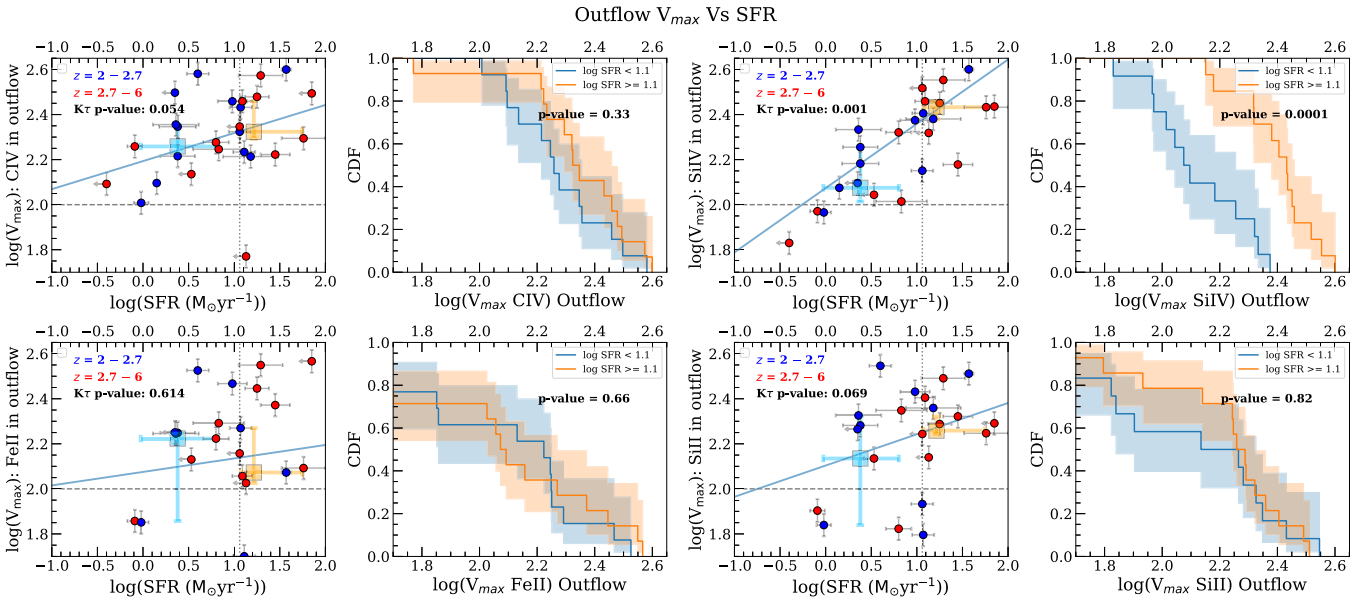


**Figure 4.** The same as Figure 3, for the maximum outflow velocity, $V_{\rm max}$ vs. SFR. The horizontal dashed line in the panels shows the 100 km s$^{-1}$ level, which we treat as the threshold for outflow.

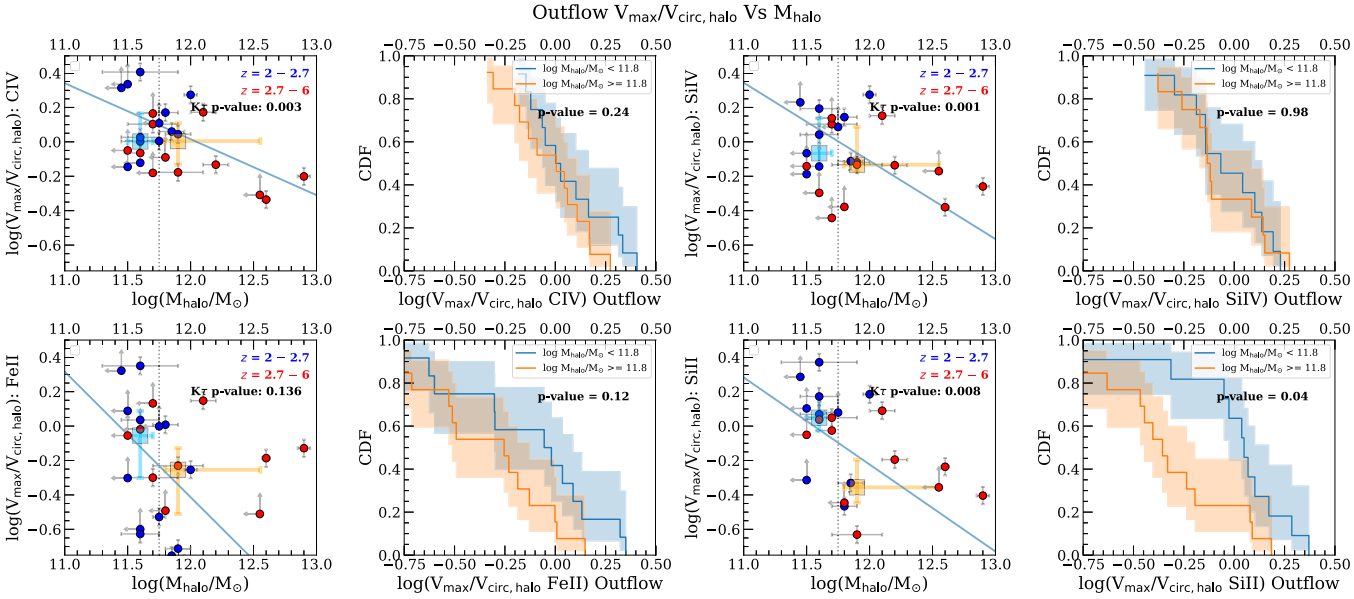


**Figure 5.** The same as Figure 3, for the normalized velocity, $V_{\rm max}/V_{\rm circ,halo}$ vs. $M_{\rm halo}$.

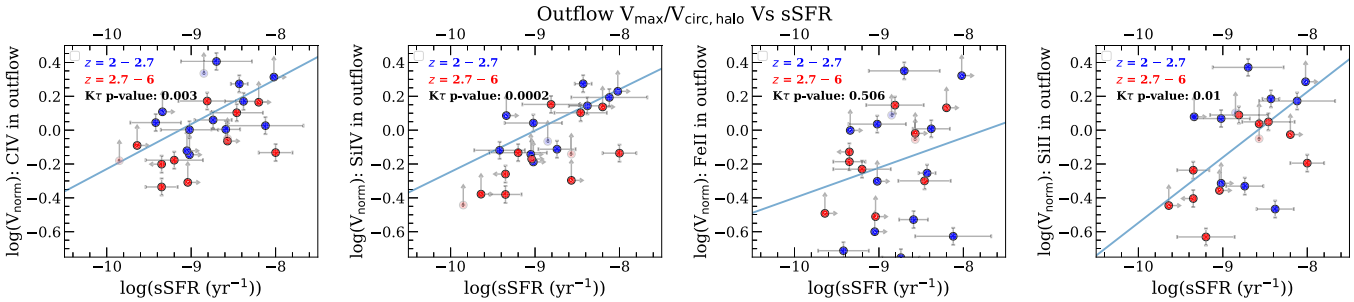


**Figure 6.** The same as Figure 15, for the the scaling relations of normalized maximum velocity ($V_{\rm max}/V_{\rm circ,halo}$) with specific SFR (=SFR/$M_*$).

$N_{\rm out}$) in the two bins are consistent with being drawn from the same population. Therefore, for this hypothesis testing, our null hypothesis is that there is no correlation between the galaxy properties and outflow properties. If the null hypothesis is true, the two samples of outflow properties (e.g., column density), split based on galaxy property (e.g., $M_*$ or SFR), are consistent

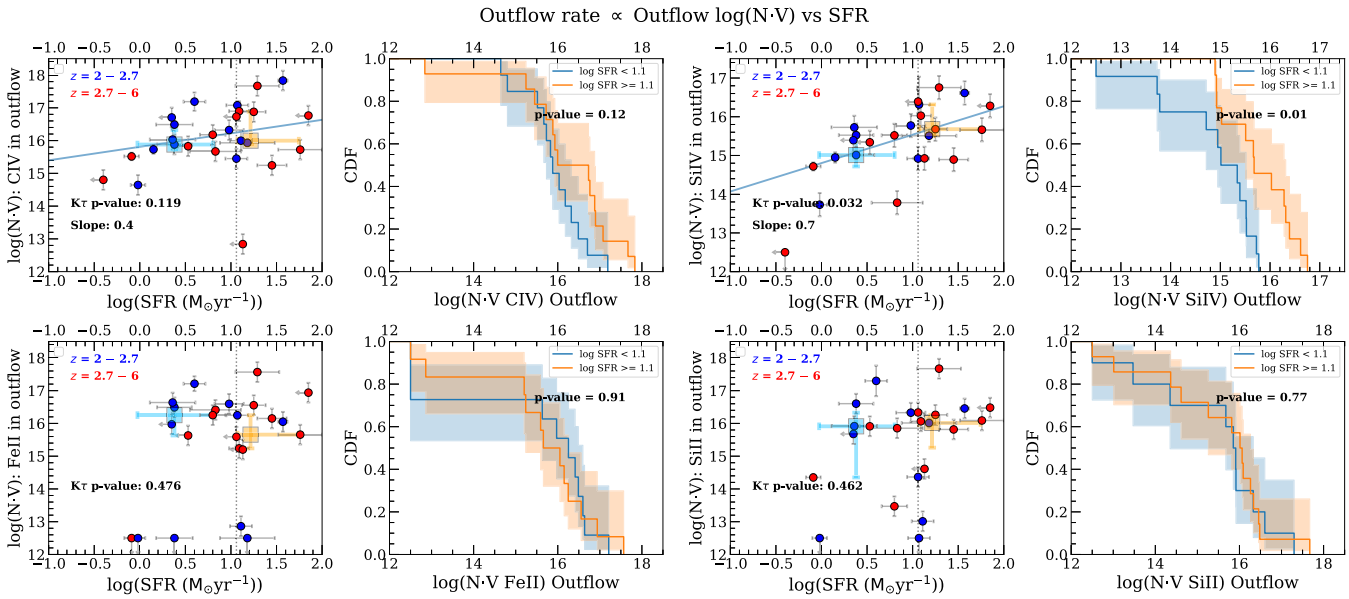


**Figure 7.** The same as Figure 3, for the relation of a proxy of outflow rate ($N{\cdot}V = \int N_a v dv$) vs. SFR. The units for the $Y$-axis are cm$^{-2}$ km s$^{-1}$. The regression fit and slope are shown where the Kendall-$\tau$ $p$-value is less than 0.15 (i.e., 1.5$\sigma$ or higher level for correlation).

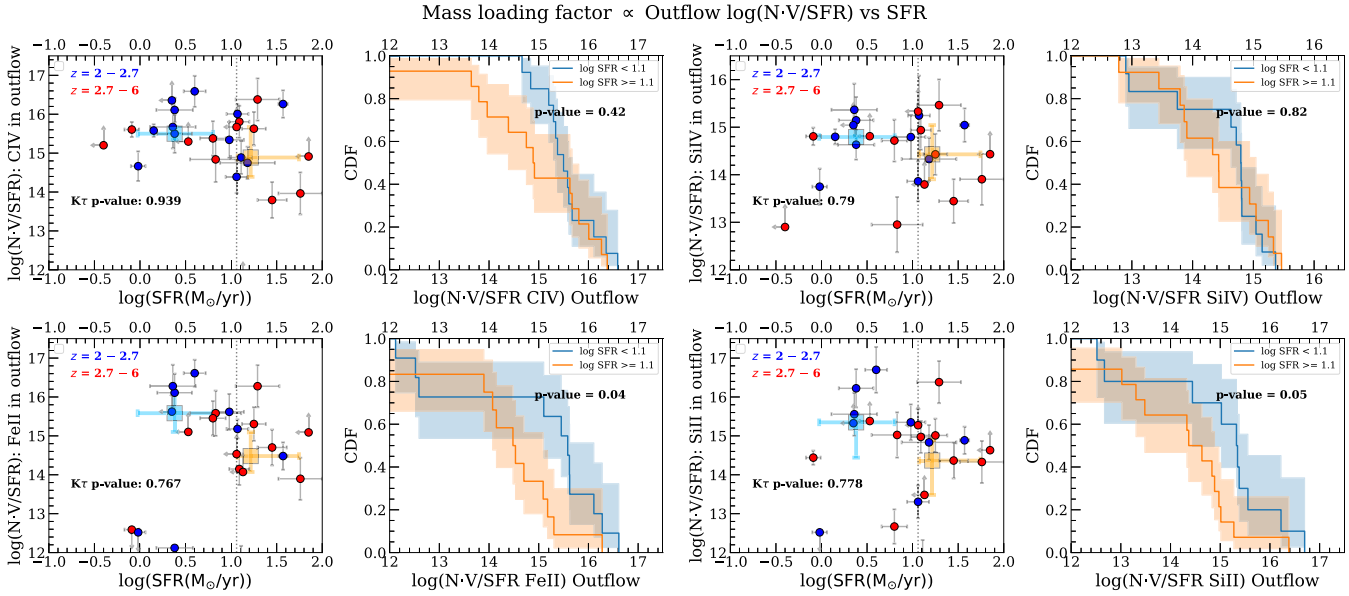


**Figure 8.** The same as Figure 3, for the relation of a proxy of mass loading factor ($N{\cdot}V/\mathrm{SFR} = \int N_a v dv/\mathrm{SFR}$) vs. SFR. The units for the $Y$-axis are cm$^{-2}$ km s$^{-1}$ $M_\odot^{-1}$ yr.

with being drawn from the same population, which would imply an absence of correlation between the given outflow property and the galaxy property.

We plot the cumulative densities of both the samples, which further visually shows the distinction or similarity between the two sample distributions. To accommodate the upper limits in our observations, we calculate the cumulative distribution function (CDF), and its spread is evaluated using a survival analysis method called the Kaplan–Meier estimator (Feigelson & Nelson 1985; Isobe et al. 1986). A python package called `lifelines` (Davidson-Pilon 2019) is used to calculate the CDF and its 1$\sigma$ spread using the Kaplan–Meier method. For two-sample hypothesis testing, we use the log-rank test in `lifelines`. The resulting $p$-values describe the probability of the two samples being drawn from the same distribution (and hence whether there is no correlation). With a stronger intrinsic correlation, the $p$-value is expected to be smaller. In Figures 3–10, the split in samples is shown with a vertical dotted line. The median of the sample on either side and its 68-percentile spread are shown in large square points for comparison (on the $X$-axis, it is the 68-percentile spread in the sample; on the $Y$-axis, it is the 68-percentile spread in the inferred median).

## 4. Outflow Correlations

In this section, we describe various outflow–galaxy correlations. A wide variety of correlations were investigated. In this section, we only describe the ones where at least one of the species shows a $\gtrsim$2$\sigma$ correlation. The rest of the correlations

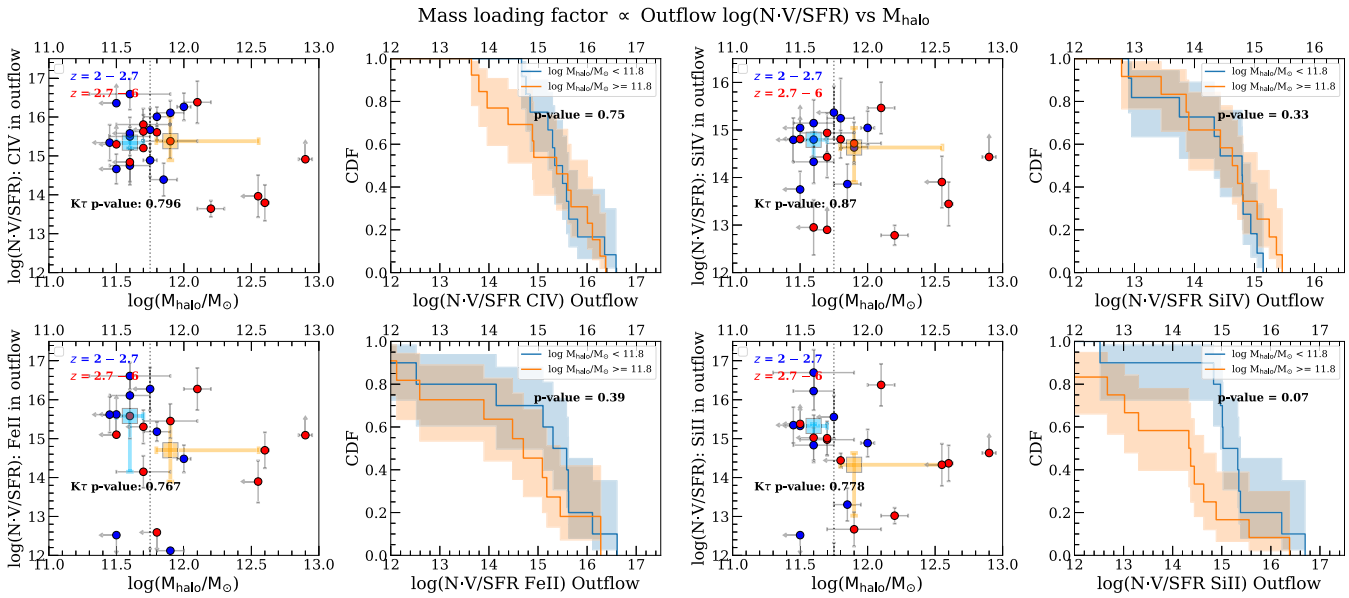


**Figure 9.** The same as Figure 3, for the relation of a proxy of the mass loading factor ($N{\cdot}V/\mathrm{SFR} = \int N_a v dv/\mathrm{SFR}$) vs. $M_{\rm halo}$. The units for the $Y$-axis are $\mathrm{cm}^{-2}$ km $\mathrm{s}^{-1}$ $M_{\odot}^{-1}$ yr.

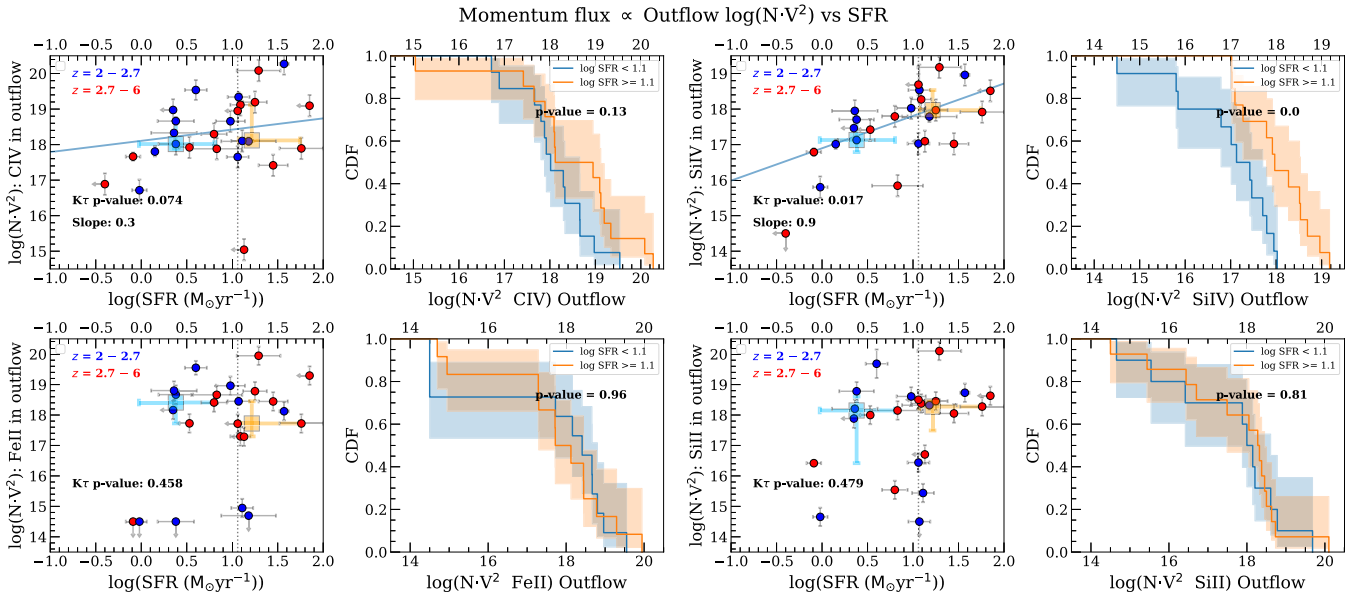


**Figure 10.** The same as Figure 3, for the relation of a proxy of momentum flux ($N{\cdot}V^2 = \int N_a v^2 dv$) vs. SFR. The units for the $Y$-axis are $\mathrm{cm}^{-2}$ $(\mathrm{km\ s}^{-1})^2$. The regression fit and slope are shown where the Kendall-$\tau$ $p$-value is less than 0.15 (i.e., $1.5\sigma$ or higher level for correlation).

are described in Appendix B for the sake of completeness and a visual comparison. All the investigated correlations are summarized in Table 3.

### 4.1. Outflow Column Density versus Galaxy Properties

In Figures 3 and 14, we plot the blue-wing column densities of C IV, Si IV, Fe II, and Si II with SFR and $M_*$, respectively. The key findings are summarized in the following subsections.

#### 4.1.1. Blue-wing Detection Fraction

We define the detection fraction as the number of objects with detected blue-wing absorption divided by the total number of objects in each sample. The detection fractions in the left and right samples in Figure 3 ($N_{\rm out}$ versus SFR) are: C IV (1 and 0.92), Si IV (0.92 and 1), Fe II (0.62 and 0.71), and Si II (0.66 and 0.77). The relative difference in the left and right samples is insignificant (i.e., contributed by an excess of one nondetection in one of the samples). We find the same result in Figure 14 ($N_{\rm out}$ versus $M_*$). Thus, we conclude that the detection fractions in the outflow do not strongly depend on the galaxy's stellar mass or SFR. However, we note that the blue-wing detection fraction is significantly higher in the high-ion species (C IV, Si IV) compared to the low-ion species, hinting at a prevalence of outflows primarily traced by the warm phase ($10^{4.5}$–$10^{5.5}$ K; Tumlinson et al. 2017; Gatkine et al. 2019), assuming collisional ionization equilibrium.

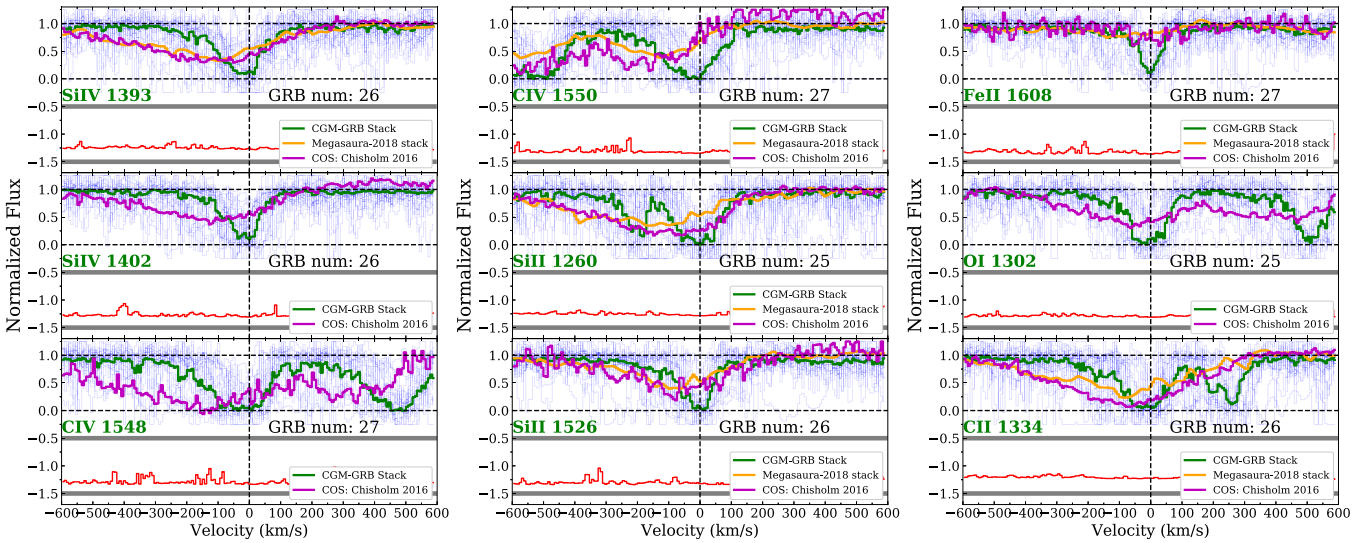


**Figure 11.** The median absorption line profiles for the CGM–GRB sample (in green) of the individual spectra (in blue) in the CGM–GRB sample. The red lines in the bottom panels show the rms noise (shifted vertically by −1.5). The overlaid traces are stacked median profiles of the MEGaSaURA $z \sim 2$ sample of 14 lensed starburst galaxies (in orange) and the $z \sim 0.1$ COS-sample of 41 starburst/star-forming galaxies (in magenta), both sourced from Rigby et al. (2018).

#### 4.1.2. $N_{out}$ versus SFR

From visual inspection of the $N_{\rm out}$ versus SFR panels in Figure 3, we note that there is a greater prevalence of high $N_{\rm out}$ in the high-SFR sample compared to the low-SFR sample. The CDF plots provide a quantitative measure of any such relation. First, we focus on the high-ion species (C IV and Si IV). The low-SFR and high-SFR samples are most distinct (i.e., small $p$-values) in high-ion species. We can reject the hypothesis of absence of correlation (between $N_{\rm out}$ versus SFR) for C IV and Si IV with 87% and 98% confidence $(1-p)$, respectively. Thus, a higher SFR is likely to be correlated with a higher column density of C IV and Si IV in the outflows (albeit with relatively lower confidence). In addition, we note that the spread of $N_{\rm out}$ (as evident from the 68-percentile errorbars on the median points) is considerably higher in the high-SFR sample compared to the low-SFR sample (by ∼0.3–0.5 dex). This effect is discussed in more detail in Section 5.4.

Unlike the case of the high-ion species, the $p$-value is high, indicating a weak (for Si II) or no correlation (for Fe II) of low-ion $N_{\rm out}$ with SFR. The fact that we see a stronger high-ion outflow with star formation but only a weak change in the low-ion species indicates that a higher SFR leads to a stronger high-ion-traced outflow, but does not significantly affect the low-ion-traced outflow phase. In other words, a higher SFR selectively enriches the outflow with high ions.

### 4.2. Outflow Kinematics and Galaxy Properties

We study the relationship between outflow kinematics and galaxy properties using the maximum velocity of the outflow (i.e., the maximum velocity in the blue wing), $V_{\rm max}$. We define $V_{\rm max}$ as the velocity of the most blueshifted absorption component + the half-power width of that component. The maximal velocity is a key determinant of the outflow energy and mass outflow rate, and hence the enrichment of the CGM (and IGM). Therefore, in this paper, we use $V_{\rm max}$ as a proxy for outflow kinematics to investigate the effect on galaxy properties.

#### 4.2.1. Outflow $V_{max}$ versus SFR

From Figure 4, a strong correlation is observed between $V_{\rm max}$ and SFR for high-ion species ($2\sigma$ for C IV and $3\sigma$ for Si IV). The best-fit relations are given by $V_{\rm max} \propto {\rm SFR}^{0.12}$ and ${\rm SFR}^{0.29}$ for C IV and Si IV, respectively. This correlation is much tighter than the SFR–column density relation. The smaller variation would mean the velocity gain due to higher SFR is mostly independent of the sightline being probed. By combining this with previous results from Section 4.1.2, it can be said that star formation uniformly drives up the high-ion outflow velocity, but also imparts a large variance in the overall amount of outflowing material (column density) that is being driven. We discuss this aspect in more detail in Section 5.4.

On the other hand, for low-ion species, the correlation is weaker (39% and 93% confidence for Fe II and Si II, respectively), primarily due to a larger spread in the $V_{\rm max}$ compared to high-ion species (which can be easily seen by comparing their CDF plots). This shows a larger variance in the kinematics of low-ion-traced outflows relative to the high-ion-traced outflows.

In addition, Figure 4 also shows that the high-redshift and the low-redshift populations (groups $z1$ and $z2$) follow the same trend for the $V_{\rm max}$–SFR correlation. We do not observe any significant evolution in the relation of outflow kinematics and SFR. This further corroborates a previous result from Gatkine et al. (2019), which shows no evolution in the CGM kinematics in the same two redshift bins.

#### 4.2.2. Outflow Kinematics versus Halo Mass

The halo mass is an important factor in determining whether the outflow will eventually escape and enrich the IGM or whether it will virialize and enrich the CGM. Therefore, it is important to understand how the outflow velocity compares with the characteristic velocity of the halo. To study how the outflow kinematics relate to the halo mass, we define a normalized velocity, $V_{\rm norm} = V_{\rm max}/V_{\rm circ,halo}$, where $V_{\rm circ,halo}$ is the halo circular velocity. The $V_{\rm circ,halo}$ is calculated using the

**Table 3**
Summary of Correlations between the CGM and Galaxy Properties Investigated for this Sample

| Outflow Property | Galaxy Property | Ion | Slope | Intercept | K−$\tau$ $p$-value | Median-split $p$-value |
|---|---|---|---|---|---|---|
| Outflow Column Density ($N_{\rm out}$) | $M_*$ | C IV | 0.23 | 12.08 | 0.20 | 0.44 |
| Outflow Column Density ($N_{\rm out}$) | $M_*$ | Si IV | 0.20 | 11.57 | 0.26 | 0.26 |
| Outflow Column Density ($N_{\rm out}$) | $M_*$ | Fe II | 0.22 | 11.91 | 0.61 | 0.88 |
| Outflow Column Density ($N_{\rm out}$) | $M_*$ | Si II | 0.18 | 12.24 | 0.80 | 0.92 |
| Outflow Column Density ($N_{\rm out}$) | SFR | C IV | 0.22 | 13.99 | 0.14 | 0.13 |
| Outflow Column Density ($N_{\rm out}$) | SFR | Si IV | 0.25 | 13.25 | 0.08 | 0.02 |
| Outflow Column Density ($N_{\rm out}$) | SFR | Fe II | 0.12 | 13.86 | 0.53 | 0.98 |
| Outflow Column Density ($N_{\rm out}$) | SFR | Si II | 0.27 | 13.65 | 0.20 | 0.53 |
| Maximum Outflow Velocity ($V_{\rm max}$) | $M_*$ | C IV | 0.07 | 1.64 | 0.16 | 0.4 |
| Maximum Outflow Velocity ($V_{\rm max}$) | $M_*$ | Si IV | 0.18 | 0.49 | 0.02 | 0.07 |
| Maximum Outflow Velocity ($V_{\rm max}$) | $M_*$ | Fe II | 0.0095 | 2.03 | 0.87 | 0.9 |
| Maximum Outflow Velocity ($V_{\rm max}$) | $M_*$ | Si II | −0.03 | 2.54 | 0.87 | 0.75 |
| Maximum Outflow Velocity ($V_{\rm max}$) | SFR | C IV | 0.12 | 2.19 | 0.05 | 0.33 |
| Maximum Outflow Velocity ($V_{\rm max}$) | SFR | Si IV | 0.28 | 2.07 | 0.0007 | 0.0001 |
| Maximum Outflow Velocity ($V_{\rm max}$) | SFR | Fe II | 0.06 | 2.08 | 0.61 | 0.66 |
| Maximum Outflow Velocity ($V_{\rm max}$) | SFR | Si II | 0.14 | 2.10 | 0.07 | 0.82 |
| Normalized Velocity ($V_{\rm max}/V_{\rm circ,halo}$) | $M_{\rm halo}$ | C IV | −0.32 | 3.92 | 0.003 | 0.24 |
| Normalized Velocity ($V_{\rm max}/V_{\rm circ,halo}$) | $M_{\rm halo}$ | Si IV | −0.45 | 5.34 | 0.0012 | 0.98 |
| Normalized Velocity ($V_{\rm max}/V_{\rm circ,halo}$) | $M_{\rm halo}$ | Fe II | −0.73 | 8.34 | 0.14 | 0.12 |
| Normalized Velocity($V_{\rm max}/V_{\rm circ,halo}$) | $M_{\rm halo}$ | Si II | −0.51 | 5.85 | 0.0085 | 0.04 |
| Outflow Column Density ($N_{\rm out}$) | sSFR | C IV | 0.12 | 15.34 | 0.66 | ⋯ |
| Outflow Column Density ($N_{\rm out}$) | sSFR | Si IV | 0.098 | 14.31 | 0.90 | ⋯ |
| Outflow Column Density ($N_{\rm out}$) | sSFR | Fe II | −0.17 | 12.59 | 0.41 | ⋯ |
| Outflow Column Density ($N_{\rm out}$) | sSFR | Si II | 0.06 | 14.30 | 0.97 | ⋯ |
| Maximum Outflow Velocity (V_max) | sSFR | C IV | 0.03 | 2.67 | 0.97 | ⋯ |
| Maximum Outflow Velocity (V_max) | sSFR | Si IV | 0.13 | 3.48 | 0.86 | ⋯ |
| Maximum Outflow Velocity (V_max) | sSFR | Fe II | 0.32 | 5.08 | 0.33 | ⋯ |
| Maximum Outflow Velocity (V_max) | sSFR | Si II | 0.21 | 4.03 | 0.34 | ⋯ |
| Normalized Velocity ($V_{\rm max}/V_{\rm circ,halo}$) | sSFR | C IV | 0.26 | 2.42 | 0.003 | ⋯ |
| Normalized Velocity ($V_{\rm max}/V_{\rm circ,halo}$) | sSFR | Si IV | 0.24 | 2.19 | 0.0002 | ⋯ |
| Normalized Velocity ($V_{\rm max}/V_{\rm circ,halo}$) | sSFR | Fe II | 0.18 | 1.38 | 0.51 | ⋯ |
| Normalized Velocity ($V_{\rm max}/V_{\rm circ,halo}$) | sSFR | Si II | 0.39 | 3.32 | 0.010 | ⋯ |
| Outflow Rate ($N{\cdot}V = \int N_a v dv$) | SFR | C IV | 0.41 | 15.81 | 0.12 | 0.12 |
| Outflow Rate ($N{\cdot}V = \int N_a v dv$) | SFR | Si IV | 0.74 | 14.80 | 0.032 | 0.01 |
| Outflow Rate ($N{\cdot}V = \int N_a v dv$) | SFR | Fe II | 0.90 | 14.40 | 0.48 | 0.91 |
| Outflow Rate ($N{\cdot}V = \int N_a v dv$) | SFR | Si II | 0.31 | 14.96 | 0.46 | 0.77 |
| Mass Loading Factor ($N{\cdot}V/{\rm SFR} = \int N_a v dv/{\rm SFR}$) | SFR | C IV | 0.39 | 14.39 | 0.94 | 0.42 |
| Mass Loading Factor ($N{\cdot}V/{\rm SFR} = \int N_a v dv/{\rm SFR}$) | SFR | Si IV | 0.59 | 13.66 | 0.79 | 0.82 |
| Mass Loading Factor ($N{\cdot}V/{\rm SFR} = \int N_a v dv/{\rm SFR}$) | SFR | Fe II | 1.47 | 12.31 | 0.77 | 0.04 |
| Mass Loading Factor ($N{\cdot}V/{\rm SFR} = \int N_a v dv/{\rm SFR}$) | SFR | Si II | 0.94 | 12.94 | 0.78 | 0.05 |
| Mass Loading Factor ($N{\cdot}V/{\rm SFR} = \int N_a v dv/{\rm SFR}$) | $M_{\rm halo}$ | C IV | −0.45 | 20.33 | 0.80 | 0.75 |
| Mass Loading Factor ($N{\cdot}V/{\rm SFR} = \int N_a v dv/{\rm SFR}$) | $M_{\rm halo}$ | Si IV | 0.05 | 13.61 | 0.87 | 0.33 |
| Mass Loading Factor ($N{\cdot}V/{\rm SFR} = \int N_a v dv/{\rm SFR}$) | $M_{\rm halo}$ | Fe II | 1.47 | 12.31 | 0.77 | 0.39 |
| Mass Loading Factor ($N{\cdot}V/{\rm SFR} = \int N_a v dv/{\rm SFR}$) | $M_{\rm halo}$ | Si II | 0.94 | 12.94 | 0.78 | 0.07 |
| Momentum Flux ($N{\cdot}V^2 = \int N_a v^2 dv$) | SFR | C IV | 0.32 | 18.11 | 0.074 | 0.13 |
| Momentum Flux ($N{\cdot}V^2 = \int N_a v^2 dv$) | SFR | Si IV | 0.91 | 16.90 | 0.017 | 0.001 |
| Momentum Flux ($N{\cdot}V^2 = \int N_a v^2 dv$) | SFR | Fe II | 0.97 | 16.54 | 0.46 | 0.96 |
| Momentum Flux ($N{\cdot}V^2 = \int N_a v^2 dv$) | SFR | Si II | 0.25 | 17.39 | 0.48 | 0.81 |
| Outflow Column Density ($N_{\rm out}$) | $M_*$ | O VI | 0.37 | 10.74 | 0.099 | 0.48 |
| Outflow Column Density ($N_{\rm out}$) | SFR | O VI | 0.06 | 14.02 | 0.70 | 0.27 |
| Maximum outflow velocity ($V_{\rm max}$) | $M_*$ | O VI | 0.06 | 1.77 | 0.35 | 0.69 |
| Maximum outflow velocity ($V_{\rm max}$) | SFR | O VI | −0.06 | 2.30 | 0.94 | 0.21 |

following equations from Mo & White (2002):

$$V_{\rm circ,halo} = \left(\frac{GM_{\rm halo}}{r_{\rm halo}}\right)^{1/2}, \quad (4)$$

$$r_{\rm halo} = \left(\frac{GM_{\rm halo}}{100\Omega_m H_0^2}\right)^{1/3}(1+z)^{-1}. \quad (5)$$

Here, $M_{\rm halo}$ is calculated using the redshift-dependent stellar-to-halo mass ratio from Wechsler & Tinker (2018).

The $V_{\rm norm}$–$M_{\rm halo}$ relation is summarized in Figure 5. We observe a clear inverse correlation in both high-ion and low-ion outflows. The inverse correlation is slightly stronger in high ions (confidence: 99.7% in C IV; 99.9% in Si IV) compared to low ions (confidence: 86.4% in Fe II; 99.2% in Si II). We note that most of the low-redshift points appear in the low-$M_{\rm halo}$ group, while the high-redshift points appear in the high-$M_{\rm halo}$ group. This is because the stellar-to-halo mass ratio is larger at higher redshifts. Also, $V_{\rm circ}$ scales as $M_{\rm halo}^{1/3}$, thus lowering the value of $V_{\rm norm}$ for the high-redshift objects.

The key takeaway from the $V_{\rm norm}$–$M_{\rm halo}$ relation is that the outflows in low-mass halos have a greater probability of reaching and/or escaping the outer CGM and enriching the IGM. Assuming that $V_{\rm max}$ reflects the gas motion at the largest radii of the outflows, as interpreted in Martin & Bouché (2009; with or without acceleration at larger radii), we can infer that outflows with $V_{\rm max} > 2 \times V_{\rm circ}$ (i.e., $\log(V_{\rm norm}) > 0.3$) are most likely to escape the CGM and enrich the IGM at high redshifts.

### 4.3. Outflow $V_{norm}$ versus Specific SFR

Following the strong $V_{\rm norm}$–$M_{\rm halo}$ relation observed in Section 4.2.2, we set out to explore whether $V_{\rm norm}$ (which is a gauge of whether the outflow can escape) is impacted by the sSFR. These results are summarized in Figure 6. We clearly observe a strong correlation between $V_{\rm norm}$ and sSFR for both high and low ions (except Fe II).

Our results are analogous to those found in Heckman & Borthakur (2016) for extreme starbursts at $z \sim 0$–$0.7$ using the Si II line. They find that $V_{\rm norm} \propto {\rm sSFR}^{0.25}$ with $>3\sigma$ confidence. Our scaling relations are consistent with this slope ($V_{\rm norm} \propto {\rm sSFR}^{0.26}$, ${\rm sSFR}^{0.24}$, ${\rm sSFR}^{0.26}$, and ${\rm sSFR}^{0.39}$ for C IV, Si IV, and Si II, with $3\sigma$, $3.7\sigma$, and $2.6\sigma$ confidence, respectively).

We note that $V_{\rm norm}$ is larger in Heckman & Borthakur (2016). This is because they study extreme starburst galaxies with typical SFRs that are higher by at least an order of magnitude compared to our sample. This leads to a 2–3× boost in outflow velocities. Regardless, the correlation is fairly robust in the sSFR range: $\log({\rm sSFR}) \sim -10$ to $-7.5$, similar to our range of interest. Given the strong agreement between the slopes obtained from the low-redshift results (Heckman & Borthakur 2016) and our high-redshift results, we argue that the $V_{\rm norm}$–SFR proportionality may be a redshift-independent fundamental property of star-forming galaxies. This should be investigated further using low- and intermediate-redshift analogs of high-$z$ star-forming galaxies.

This is the first such evidence of $V_{\rm norm}$–SFR correlation at $z > 2$. The combined $V_{\rm norm}$–SFR and $V_{\rm norm}$–$M_{\rm halo}$ relations (Section 4.2.2) imply that the outflows from the low-mass halos and high-sSFR galaxies have the highest probability of escaping the halo and transferring matter to the IGM, and thus enriching it with metals.

### 4.4. Outflow Rate and Mass Loading Correlations

Assuming a spherical outflow geometry, the time-averaged mass outflow rate ($\dot{M}_{\rm out}$) across a cross-sectional area $A$ (over a dynamical timescale $\sim R/V_{\rm mean}$) can be written as

$$\dot{M}_{\rm out} = m\frac{A}{R}\int N_a(v_{\rm out})v_{\rm out}dv, \quad (6)$$

where $m$ is the mean atomic mass per H atom, $R$ is the radius at which the cross section is evaluated, and $N_a(v)$ is the apparent column density (per unit velocity) at a velocity $v$.

Here, we use the observable parameter $\int N_a(v_{\rm out})v_{\rm out}dv$ (abbreviated as $N{\cdot}V$) as a proxy for the mass outflow rate, since the radial profile of the outflow is unknown. We use the best-fit Voigt profiles for the spectra in our sample, as derived in Gatkine et al. (2019), and evaluate $N_a(v_{\rm out})$ using the apparent optical depth method (Savage & Sembach 1991; also see Section 4.2 in Gatkine et al. 2019). The integration is performed leftward of $v = -100$ km s$^{-1}$ to consider only the outflows. We note that using the $N{\cdot}V$ of various high- and low-ion species as the proxy for $\dot{M}_{\rm out}$ has certain limitations. The ionization fraction of the species, the metallicity of the outflow, and the outflow geometry can vary within the redshift range and as a function of galaxy properties. Despite these variations, the $N{\cdot}V$ provides a useful insight into the comparative outflow dynamics of the high-ion- and low-ion-traced outflows. Keeping these strengths and limitations in mind, we investigate the following correlations to trace the outflow dynamics.

#### 4.4.1. Outflow Rate versus SFR

In Figure 7, we plot $N{\cdot}V$ (a proxy for the mass outflow rate) against SFR. We observe an increasing trend in the high ions (C IV and Si IV) with an approximate log–log slope of $\sim 0.5$, suggesting that the mass outflow rate of high-ion-traced outflows is driven by star formation. However, we do not observe such a trend in the low ions. This is expected, given the large scatter (or absence) of $N_{\rm out}$ and $V_{\rm max}$ correlations with SFR in the low-ion species.

The high-ion correlation has a slope ($0.4-0.7$; see Figure 7) slightly shallower than the slope obtained by Heckman et al. (2015; ($\log(\dot{M}_{\rm out})$–$\log({\rm SFR})$) slope of $\sim 1$) for local starbursts using both high- and low-ion lines, albeit with a larger scatter (see Figure 5 in their paper). Chisholm et al. (2015) also find a similar correlation (slope of $\sim 0.5$) in a sample of local star-forming galaxies using low-ion lines. These similarities indicate a common star formation-driven outflow mechanism from $z \sim 0$ to $z \sim 6$. We note here, however, that the marked difference that we see between the high- and low-ion correlations implies a systematic difference in the outflow mechanisms of the phases traced by them. The blue wings in the high-ion absorption appear to be dominated by outflows driven by star formation (as supported by the correlations), while the blue wings in the low ions are more complex.

To gauge how the mass outflow rate compares with the star formation of the sample, we take C IV species as an example and estimate the total outflow rate as follows:

$$\dot{M}_{\rm out,H} = \dot{M}_{\rm out,C\,IV}\frac{1}{f_{\rm C\,IV}Z_{\rm out}}\left(\frac{N_{\rm H}}{N_{\rm C}}\right)_{\rm solar}. \quad (7)$$

Here, $f_{\rm C\,IV}$ is the ionization fraction of C IV, $Z_{\rm out}$ is an estimate of the outflow metallicity, and $N_{\rm C}/N_{\rm H}$ is the carbon

abundance (Lodders 2003). Using Equations (6) and (7),

$$\dot{M}_{\rm out} \approx 1\ M_\odot\ {\rm yr}^{-1}\left(\frac{(N.V)_{\rm C\,IV}}{10^{16.5}\ {\rm cm}^{-2}\ {\rm km\ s}^{-1}}\right)\left(\frac{5\ {\rm kpc}}{R_{\rm out}}\right) \times \left(\frac{0.3}{f_{\rm C\,IV}}\right) \times \left(\frac{0.25}{Z_{\rm outflow}}\right)\left(\frac{2.8\times10^{-4}}{(N_{\rm C}/N_{\rm H})_\odot}\right). \quad (8)$$

Here, a representative $N{\cdot}V$ value is taken for C IV species at SFR $\sim 10\ M_\odot\ {\rm yr}^{-1}$ (see Figure 7). There is a scatter of about an order of magnitude in either direction in the observed $N{\cdot}V$ values for C IV. The values of $Z_{\rm outflow}$ and $f_{\rm C\,IV}$ are assumed to be the same as those in Gatkine et al. (2019), and the radius of the outflowing shell is assumed to be 5 kpc. Note that this mass outflow rate is a lower limit, given the conservative assumptions of the C IV ionization fraction (see Section 6.1.2 in Gatkine et al. 2019 for a detailed explanation) and outflow radius. The measured outflow properties can arise from a radius as large as 50 kpc (i.e., the typical virial radius of these galaxies). Thus, the $\dot{M}_{\rm out}$ estimated in Equation (8) can be larger by almost an order of magnitude. Regardless, given the scatter in the observed $N{\cdot}V$, many of the observed systems have an estimated mass outflow rate comparable to or even greater than the SFR.

Given that $N{\cdot}V \propto {\rm SFR}^{0.4}$ for C IV (or ${\rm SFR}^{0.7}$ for Si IV), it is evident that the lower-SFR galaxies in our sample experience a higher mass outflow rate as a fraction of their SFR, and thus undergo an efficient removal of the gas compared to high-SFR galaxies.

#### 4.4.2. Mass Loading Factor

Similar to Section 4.4.1, we use $N{\cdot}V/{\rm SFR}$ as the proxy for the mass loading factor ($\eta = \dot{M}_{\rm out}/{\rm SFR}$) to measure how efficiently the galaxy removes gas (in comparison to SFR). We study its relation with SFR and $M_{\rm halo}$ in Figures 8 and 9, respectively, to understand the potential drivers of the mass loading factor.

For the $\eta$ versus SFR plot (Figure 8), we do not find a clear correlation. However, by splitting the sample into two equal high-SFR and low-SFR bins, and comparing the medians, we observe a declining trend with SFR. This suggests a higher outflow efficiency in the low-SFR galaxies, particularly for the outflows traced by low-ion lines. We note that this result has to be seen in conjunction with the $N{\cdot}V$ versus SFR plot (Figure 7). The weaker decline in the high ions is driven by the intrinsic correlation between $N{\cdot}V$ and SFR. On the other hand, the stronger decline seen in the low ions is due to the lack of such an intrinsic $N{\cdot}V-$SFR correlation, leaving the $1/{\rm SFR}$ as the dominant term. The observed slow decline in the high ions is in agreement with the simulated slope for stellar feedback ($\eta \sim {\rm SFR}^{0.35}$ for winds leaving the ISM) in the star-forming galaxies at $z > 2$ in the EAGLE simulations (Mitchell et al. 2020; see Figure 3 therein).

In the $\eta$ versus $M_{\rm halo}$ plot (Figure 9), we observe a large scatter in this relation, and thus we cannot find any statistically significant correlation for either low- or high-ion species. The large scatter in this relation makes a comparison with cosmological simulations difficult. There is a possible hint of a declining outflow efficiency at high halo masses, particularly for the low ions (as seen from the binned sample), but a significantly larger sample will be needed in the future to constrain any underlying correlation.

#### 4.4.3. Momentum Flux versus SFR

The stellar processes (supernovae and stellar winds) can drive momentum flux as a combination of both radiation pressure (Murray et al. 2005) and ram pressure of a hot outflow collectively created from the ejecta of massive stars (Chevalier & Clegg 1985; Veilleux et al. 2005; Heckman & Borthakur 2016). Similar to Equation (6), the time-averaged momentum flux across a cross-sectional area $A$ (over a dynamical timescale $\sim R/V_{\rm mean}$) can be written as:

$$\dot{p}_{\rm out} = m\frac{A}{R}\int N_a(v_{\rm out})\,v_{\rm out}^2\,dv. \quad (9)$$

We use the observable parameter $\int N_a(v_{\rm out})\,v_{\rm out}^2\,dv$ (abbreviated as $N{\cdot}V^2$) as a proxy for the momentum flux. In Figure 10, we plot $N{\cdot}V^2$ against SFR. We observe a correlation for high ions: $\dot{p}_{\rm out} \propto {\rm SFR}^{0.3}$ for C IV and ${\rm SFR}^{0.9}$ for Si IV, with a stronger correlation for Si IV. However, we find no correlation for the low ions. This is expected, given the strong correlation between $V_{\rm max}$ and SFR for high -ions observed in Section 4.2.1, and the lack of such a correlation for low ions.

Next, we compare the momentum flux with star formation-driven momentum flux to examine whether it is sufficient to drive the observed momentum flux in the high-ion-traced outflows. For a standard Kroupa/Chabrier initial mass function and a constant SFR, the estimated stellar-driven momentum flux is given by the sum of radiation pressure and ram pressure components (Heckman et al. 2015) as:

$$\dot{p}_* = 4.8\times10^{33}\ {\rm dynes}\times{\rm SFR\ (in}\ M_\odot\ {\rm yr}^{-1}). \quad (10)$$

To compare this with the observed momentum flux, we use C IV ion as a probe and rewrite Equation (9) as follows:

$$\dot{p}_{\rm out} = 5\times10^{32}\ {\rm dynes}\left(\frac{N.V^2}{10^{18.5}\ {\rm cm}^{-2}\ {\rm km}^2\ {\rm s}^{-2}}\right)\left(\frac{0.3}{f_{\rm C\,IV}}\right) \times \left(\frac{0.25}{Z_{\rm outflow}}\right)\left(\frac{2.8\times10^{-4}}{(N_{\rm C}/N_{\rm H})_\odot}\right). \quad (11)$$

Here, a representative $N{\cdot}V^2$ value is taken for C IV species at SFR $\sim 10 M_\odot\ {\rm yr}^{-1}$ (see Figure 10). There is a scatter of about an order of magnitude in either direction in the observed $N{\cdot}V^2$ values for C IV. The values of $Z_{\rm outflow}$ and $f_{\rm C\,IV}$ are assumed to be the same as those in Gatkine et al. (2019), and the radius of the outflowing shell is assumed to be 5 kpc. We issue the same caution as in Section 4.4.1 about this estimate being a lower limit, given the conservative assumptions of C IV ionization fraction and outflow radius.

Despite the scatter in the observed $N{\cdot}V^2$, it is clear that the estimated momentum flux (from Equation (11)) is smaller than that driven by star formation (from Equation (10)). Thus, it is evident that the observed high-ion-traced outflows are primarily driven by the momentum directly injected by supernovae and stellar winds. This is different from the results for the low-redshift starburst and star-forming galaxies (Heckman et al. 2015 and Chisholm et al. 2017, respectively), where the momentum flux in the outflows is comparable to or even greater than that imparted by star formation for a significant fraction of the sample. However, the slope of the $N{\cdot}V^2$–SFR (or $\dot{p}_{\rm out}$–SFR) correlation for high-ions (particularly Si IV) is consistent with the local starburst result from Heckman et al. (2015). In the future, we will perform detailed ionization modeling to further examine these correlations.

## 5. Discussion

### 5.1. Star Formation-driven Outflow

The strong correlation of the blue-wing column density and maximum outflow velocity with SFR, as seen in Figures 3 and 4, provides important evidence for a star formation-driven outflow. If we consider Si IV as the outflow tracer, the best-fit lines suggest $N_{\rm Si\,IV} \propto {\rm SFR}^{0.25}$ and $V_{\rm max,Si\,IV} \propto {\rm SFR}^{0.29}$. Our $V_{\rm max}$ slope is in close agreement with the slope derived in Sugahara et al. (2017) for $z \sim 2$ star-forming galaxies (=0.25).

Similarly, the (weak) trends of high-ion column density and $V_{\rm max}$ with $M_*$ are consistent with the previous observations of C IV-traced outflows from Du et al. (2018) at $z \sim 1$–1.35. However, our sample extends to 0.4 dex lower mass, where we start to see a systematic decline in $N_{\rm out}$ as well as $V_{\rm max}$, which is not seen in these previous observations. We argue that this decline is driven by the lower SFRs. Similarly, the large spread (in $N_{\rm out}$ and $V_{\rm max}$) observed at $\log(M_*/M_\odot) > 9.4$ is due to the large spread in SFR at this mass range in our sample, as shown in Figure 2. Hence, we conclude that the apparent trends between $V_{\rm max}$ or $N_{\rm out}$ and $M_*$ are almost entirely modulated by the SFR.

For low-ion outflows, the best-fit relation for Si II is $V_{\rm max,Si\,II} \propto {\rm SFR}^{0.14}$. Various surveys from low to high redshifts have reported correlation between some form of $V_{\rm max}$ for low-ion species and SFR. Our results agree with the slopes observed in Weiner et al. (2009), Bradshaw et al. (2013), Bordoloi et al. (2014), and Chisholm et al. (2015) with redshifts ranging from $z \sim 0$–1.6. Our correlations also qualitatively agree with the $z \sim 0.5$ sample of Rubin et al. (2014; only for their galaxies without systemic absorption). From the $V_{\rm max}$–SFR slope derived here, we further corroborate the suggestion from Sugahara et al. (2019) that the $V_{\rm max}$–SFR could be a more fundamental relation over a wide redshift range ($z \sim 0$–6) for star-forming main sequence. However, we caution that there is a significant spread in the relation, depending on the species used for deriving them (for instance, we get a slope of 0.29 for Si IV and 0.14 for C IV).

Both Erb et al. (2012) and Rubin et al. (2012) find a strong correlation of $V_{\rm max}$ with stellar mass and a weak correlation with SFR for galaxies of similar mass and SFR ranges to our sample in the redshift ranges $z \sim 1$–2 and $z \sim 0.3$–0.7, for low-ion species. Similarly, Bordoloi et al. (2014) and Chisholm et al. (2015) find a high-significance correlation with $M_*$ using Mg II and Si II species, respectively. Rubin et al. (2012) argue that this could be because star formation history and/or galaxy dynamics have a more direct physical link to maximum wind velocities than current star formation activity. However, we find that the trends flip—there is a stronger correlation with SFR compared to stellar mass (for instance, consider Si II in Figures 4 and 16). This indicates that for low-mass galaxies at $z > 2$, the current star formation has a greater impact on the observed low-ion outflows than their star formation history. This is interesting from the perspective of causal connection. The timescale required for a 250 km s$^{-1}$ outflow to travel 50 kpc (roughly the virial radius of typical galaxies at $z \sim 3$) is about 200 Myr, while the UV-based SFR that we measure is from the past 100 Myr. This could indicate a long-lasting star formation activity. This is in line with our typical depletion timescale of 500 Myr (using $(M_{\rm gas} \sim M_*)/{\rm SFR} \sim 1/{\rm sSFR}$).

We compare our scaling relations with the recently published results from the TNG50 simulations (Nelson et al. 2019). We find that the slopes of our $V_{\rm max}$–SFR relation (for both high and low ions, with a slope of $\sim 0.12-0.28$) are consistent with the slope of 0.15–0.2 in Nelson et al. (2019; see Figure 15 therein). However, our results do not fully agree with the predicted $V_{\rm max}$–$M_*$ relation. While their slope of 0.2 at $z = 2$ is consistent with our high-ion results (slope = 0.19 for Si IV), Nelson et al. (2019) show a slope that steepens with redshift (e.g., slope = 0.3 at $z = 4$). We do not observe such steepening in our $V_{\rm max}$–$M_*$ plots (Figure 16). In fact, the slope appears to be shallower in the high-redshift group (group $z2 \sim 2.7$–6). This discrepancy may be explained by a combination of two factors: (a) the increasing contribution of hotter phases in the outflow with increasing $M_*$ (see Figure 10 in Nelson et al. 2019); and (b) the outflow scaling relations shown in Nelson et al. (2019) include all the phases, while our observations might only cover the warm phases for high ions (assuming collisional ionization equilibrium).

Given the strong $N_{\rm out}$–SFR and $V_{\rm max}$–SFR correlations, particularly for high-ion outflows, it is expected that the mass outflow rate would be strongly correlated with SFR. In Section 4.4.1 and Figure 7, we use $N{\cdot}V$ ($=\int N_a(v_{\rm out}) v_{\rm out} dv$) as a measure of the mass outflow rate and obtain the following relations:

$$\dot{M}_{\rm out} \propto {\rm SFR}^{0.4} \text{ for C IV}$$
$$\dot{M}_{\rm out} \propto {\rm SFR}^{0.7} \text{ for Si IV}. \quad (12)$$

The slope obtained here is in good agreement with the slope observed in the FIRE simulations ($\sim 0.6$) at $4 > z > 2$ with the rate evaluated at $0.25R_{\rm vir}$ (see Figure B2 in Muratov et al. 2015). This slope is also consistent with the EAGLE simulations at a similar redshift range ($z \sim 2.4$–4.7) for gas particles ejected out of the ISM through galactic winds (see Figure 3 in Mitchell et al. 2020). Both of these slopes have been obtained in the log(SFR) range of $-0.5$–1.5, similar to our SFR range.

### 5.2. Stacking Comparison with Previous Studies

We compare the stacked profiles of the high- and low-ion species in the CGM–GRB sample against the publicly available stacks of high- and low-redshift down-the-barrel outflow studies from Rigby et al. (2018). This includes a $z \sim 2$ sample of 14 gravitationally lensed starburst galaxies (the MEGaSaURA sample) and a sample of 41 starburst/star-forming (majority starburst) at $z \sim 0.1$ (the COS-sample; Chisholm et al. 2016).

We observe that the outflows in both the MEGaSaURA and COS-sample stacks—which consist of starbursts (SFR $\sim 10\times$ main sequence) at their respective redshifts—are considerably broader and stronger compared to the CGM–GRB sample, where the majority of the galaxies are $\sim 0.5$ dex below the main sequence at their respective redshifts (see Figure 2). Further, we note that the galaxies in the $z \sim 0.1$ COS-sample have a similar $M_*$ and SFR to our CGM–GRB host galaxies at $z > 2$ (see Chisholm et al. 2016), yet the COS-sample outflows are significantly stronger and broader than the CGM–GRB outflows for both high and low ions. This shows that, over a broad redshift range, the strength of the outflow is correlated with the main-sequence offset at the respective redshifts, rather than the simple SFR. This should be a critical consideration while comparing outflow samples at different redshifts.

On the other hand, the MEGaSaURA sample galaxies have a similar redshift range ($z \sim 1.68-3.6$) to our CGM–GRB

sample, but are significantly above the main sequence (and hence, starburst). Similar to the COS-sample, their outflows are significantly broader in velocity and stronger in absorption depth for both high and low ions. This comparison further corroborates that the SFR-driven outflows are strongly correlated with the main-sequence offset at the respective redshifts.

We should, however, caution that a direct stacking comparison of the line profiles with previous down-the-barrel samples in the literature is an unfair comparison for several reasons. The most important is the selection effect. By definition, down-the-barrel samples at $z > 2$ are selected to be galaxies bright enough in rest-frame UV for absorption spectroscopy ($g_{\rm AB} < 21$, for MEGaSaURA). On the other hand, the GRB hosts in our sample are faint, with apparent magnitude $> 23$ in most cases. In fact, the low-mass, low-SFR galaxies at high-$z$ are extremely difficult to probe at high resolution using the down-the-barrel technique. However, GRB sightlines offer a unique opportunity to probe this population, which is not feasible at scale by any other method.

Lastly, due to a combination of the selection effect and galaxy properties, the down-the-barrel observations at high-$z$ preferentially look directly down the outflows. The GRB sightlines, on the other hand, are random. These reasons also contribute to the marked difference seen in the stacks of the CGM–GRB sample and the down-the-barrel high-$z$ stacks (e.g., MEGaSaURA), and should be studied in detail in the future.

### 5.3. Evidence for High-ion-traced Outflows

We observe three key differences between high-ion and low-ion outflows. (1) The detection fraction of low-ion outflows is lower than high-ion outflows (∼65% versus 95%), irrespective of the SFR. (2) The correlations of high-ion $N_{\rm out}$ and $V_{\rm max}$ with SFR are stronger compared to low ions (see Figures 3 and 4). Also, the spread in $V_{\rm max}$ is higher in low ions. (3) Low-ion outflows show a much steeper decline in $V_{\rm norm}$ with higher halo masses compared to high-ion outflows (see Figure 5). These differences point toward a systematic difference in the high-ion and low-ion outflows. In addition, we can infer that the outflows in our sample are primarily traced by high ions.

It is well known that galactic outflows are multiphase in nature, and the aforementioned differences can help understand the phase structure of the outflows. Cosmological simulations find a complex shift in the temperature distribution of the outflow, with the dominant phase shifting toward higher temperatures as the stellar mass increases at $z \sim 2$ (see Figure 10 in Nelson et al. 2019). This trend is also seen in FIRE simulations, with the contribution of the $T > 10^{5.3}$ K phase increasing and that of the $10^4 < T < 10^{4.7}$ K phase decreasing with an increasing halo mass at $z \sim 2$ (in the range $M_{\rm halo} \sim 10^{11}$–$10^{12}$ $M_\odot$; see Figure A1 in Hafen et al. 2019). These effects can potentially explain the sharp decline in low-ion $V_{\rm norm}$ and their weaker and shallower correlations in terms of $N_{\rm out}$. Photoionization modeling of the observations would help in understanding whether this explanation is correct. Regardless, we infer that the correlations seen in the star-forming galaxies using random, narrow sightlines (as offered by GRBs) imply high-ion-dominated outflows in the star-forming galaxies at $z > 2$.

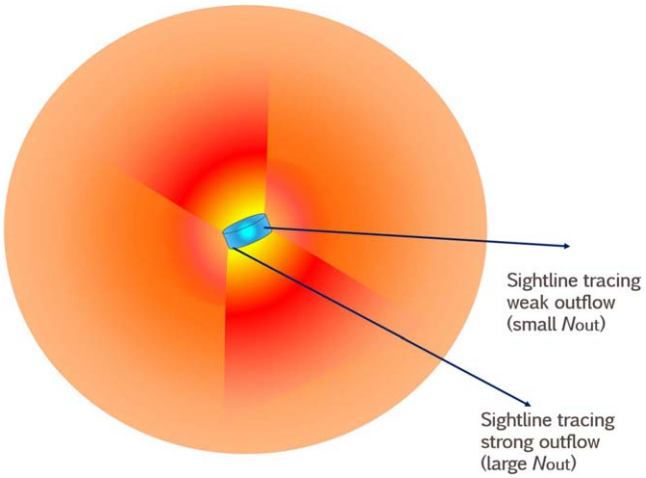


**Figure 12.** A schematic showing a stronger biconical outflow along the minor axis and weaker spherical outflow elsewhere. The narrow GRB sightlines are shown as arrows. Some of the narrow and randomly pointed GRB sightlines will trace the strong biconical outflow, giving a larger outflow column density, while others will trace the weaker outflow, giving a smaller outflow column density. This will produce a scatter in the $N_{\rm out}$–SFR relation.

### 5.4. Outflow Geometry

The sharp increase in the spread of outflow column density at SFR $\gtrsim 10$ $M_\odot$ yr$^{-1}$, particularly for high-ion lines, is an indication of systematic variance in the outflow properties with SFR.

There are various possible causes that could lead to an elevated spread in the apparent outflow column density. Some of the scenarios include a variance in the metallicity of the outflowing clouds due to the inefficient mixing of metals (Schaye et al. 2007), a variance in the entrainment efficiency of the ISM, or the onset of wind-stimulated condensation in the CGM (see Heckman et al. 2017) at high SFRs. A more careful treatment of the physical processes in the outflows is warranted to explain this phenomenon.

Another possible explanation for such a variance is outflow geometry. Given that GRBs sample a very narrow beam in a random direction offset from the galactic center, a spherical outflow is less likely to lead to the observed spread. In a nonspherical outflow, with certain regions of high gas entrainment efficiency compared to others (e.g., a biconical outflow), there will be preferred sightlines that exhibit high column density, and others will exhibit a relatively lower column density. This is illustrated in Figure 12. In addition, projection effects become more important in a nonspherical outflow as opposed to a spherical outflow. Therefore, we speculate that the increased spread could indicate the development of a nonspherical outflow in the high-SFR systems, with the low-SFR galaxies having more uniform/spherical outflows.

Such a development of outflow collimation naturally (hydrodynamically) emerges in the recent TNG simulation results along the minor axis of the galaxy, despite isotropic injection of the stellar feedback (Nelson et al. 2019). Thus, they come to a similar conclusion in their simulations: the mass outflow rate of winds is not directionally isotropic, even for $M_* = 10^{10}$ $M_\odot$ at $z = 1$. While they suggest that the effect is more pronounced as we go below $z \sim 2$, due to the rise of ordered rotation (and resulting emergence of galactic disks), it will be interesting to probe how this effect evolves in the redshift–SFR space.

### 5.5. Evolution with Redshift

While we see that $V_{\rm max}$ for high-ion lines is correlated with SFR and $M_*$, we do not observe any systematic evolution in $V_{\rm max}$ in our two redshift groups ($z1$: 2–2.7 and $z2$: 2.7–6). This is consistent with a weak or no evolution ($V_{\rm max} \sim (1+z)^{0.5}$), as suggested in Sugahara et al. (2017, 2019). However, we do not observe as high $V_{\rm max}$ values as seen in these studies. It is possible that this discrepancy is due to the small sample size (seven galaxies) in Sugahara et al. (2019), or due to the difference in observational techniques (down-the-barrel versus GRB sightlines).

## 6. Summary

We explored the outflow–galaxy correlations in low-mass ($M_* \sim 10^9$–$10^{11}$ $M_\odot$), star-forming galaxies at $z \sim 2$–6 using GRB sightline spectroscopy. This technique offers a narrow, off-centered, and randomly oriented sightline as opposed to a broad, down-the-barrel beam to probe the outflows in absorption. We summarize our results as follows:

1. SFR-driven outflows: we find strong correlations between outflow column density ($N_{\rm out}$), outflow maximum velocity ($V_{\rm max}$), and SFR. This correlation is stronger for high-ion outflows compared to low-ion outflows.
2. Correlation with $M_*$: we find a large spread and, therefore, weaker correlations of $N_{\rm out}$ and $V_{\rm max}$ in high-ion outflows with stellar mass. We find that this spread is almost entirely driven by the spread in SFR in a given stellar mass bin. On the other hand, we find that low-ion outflows are not correlated with stellar mass.
3. We observe a higher detection fraction in high ions compared to low ions (irrespective of the SFR or $M_*$), as well as typically higher $V_{\rm max}$ and $N_{\rm out}$ in high ions, indicating that the outflow is dominated by the phase traced by high-ionization lines.
4. We investigated how the normalized velocity ($V_{\rm norm} = V_{\rm max}/V_{\rm circ,halo}$) depends on the halo mass ($M_{\rm halo}$). We find a decline in $V_{\rm norm}$ with increasing halo mass, and thereby infer that the outflows from the low-mass halos are more likely to escape and enrich the outer CGM and/or IGM than those in the halos of higher masses. We also observe a steeper decline in $V_{\rm norm}$ for low ions, potentially hinting toward a systematic shift in the temperature distribution of the outflow as the halo mass increases.
5. sSFR and metal enrichment: while neither $N_{\rm out}$ nor $V_{\rm max}$ are correlated with sSFR, we observe a strong correlation between $V_{\rm norm}$ ($=V_{\rm max}/V_{\rm circ,halo}$) and sSFR at the $3\sigma$ and $3.7\sigma$ levels for C IV and Si IV, respectively, with $V_{\rm norm} \propto {\rm sSFR}^{0.25}$. This power law is consistent with the low-redshift results from Heckman & Borthakur (2016). From this result, we infer that the outflows in galaxies with higher sSFR have higher velocities relative to the characteristic velocity of their halos. Thus, the outflows from high-sSFR galaxies are more likely to escape and enrich the outer CGM and IGM compared to low sSFR galaxies.
6. Outflow dynamics: using $N{\cdot}V$ and $N{\cdot}V^2$ as proxies for $\dot{M}_{\rm out}$ and $\dot{p}_{\rm out}$, respectively, we find that they are both correlated to the SFR for the high-ion-traced outflows. We do not find such a correlation for the low ions. While the high-SFR galaxies have a higher outflow rate, the low-SFR galaxies are more efficient in driving outflows normalized to their SFRs. In addition, we find that the estimated momentum flux of the outflow can easily be supported by the momentum injected by stellar process (i.e., supernovae and stellar winds). This, in concert with the observed correlations, implies that the blue wings in the high-ion absorption are dominated by star formation-driven outflows.
7. Redshift evolution: we do not observe any systematic difference in the $V_{\rm max}$–SFR and $N_{\rm out}$–SFR correlations (for high ions) in our two redshift groups ($z1$: 2−2.7 and $z2$: 2.7–6) of similar size. This suggests that the correlations of the outflow with SFR do not significantly evolve with redshift, and are more fundamental in nature.
8. Stacking comparison: by comparing the stacks of our CGM–GRB sample with the down-the-barrel studies of starbursts at $z \sim 2$ (MEGaSaURA) and at $z \sim 0.1$ (COS-sample) in Section 5.2, we find that over a broad redshift range, the strength of the outflow is correlated with the main-sequence offset at the respective redshifts, rather than the simple SFR.
9. Structure of the outflow: we observe a larger spread in the high-ion correlation with SFR beyond an SFR of $\sim$10 $M_\odot$ yr$^{-1}$. We speculate that this spread could arise due to an emergence of nonspherical outflows (e.g., biconical) at high SFRs, leading to some sightlines cutting across a larger section of the outflow, with others probing a weaker outflow. This characteristic can be uniquely probed using the GRB sightline technique, due to the random orientation (i.e., not down the barrel) and narrow beam of the sightline (as shown in Figure 12). However, a more detailed investigation of the physical processes in the outflows is needed to explain the observed spread in the outflow column densities at high SFR.

These results highlight the unique potential of GRB afterglow spectroscopy to explore the nature and importance of stellar feedback at high redshifts.

The authors are grateful to Drs. A. Cucchiara and V. Toy for their useful comments in the early stages of this paper. P.G. was supported by a NASA Earth and Space Science Fellowship (ASTRO18F-0085), a NASA Hubble Fellowship (HST-HF2-51478.001-A), and a David & Ellen Lee Fellowship at Caltech for this research. S.V. acknowledges partial support from the National Science Foundation under grant 1711377 and National Aeronautics and Space Administration under grants 16-APRA 16-0064 and ADAP NNX16AF24G.

These results made use of the Lowell Discovery Telescope (LDT) at Lowell Observatory. Lowell is a private, nonprofit institution dedicated to astrophysical research and public appreciation of astronomy, and it operates the LDT in partnership with Boston University, the University of Maryland, the University of Toledo, Northern Arizona University, and Yale University. The Large Monolithic Imager was built by Lowell Observatory using funds provided by the National Science Foundation (AST-1005313).

Based on observations made with ESO Telescopes at the La Silla Paranal Observatory under program IDs 177.A-3016, 177.A-3017, 177.A-3018, and 179.A-2004, and on data products produced by the KiDS consortium. The KiDS production team acknowledges support from: Deutsche Forschungsgemeinschaft,

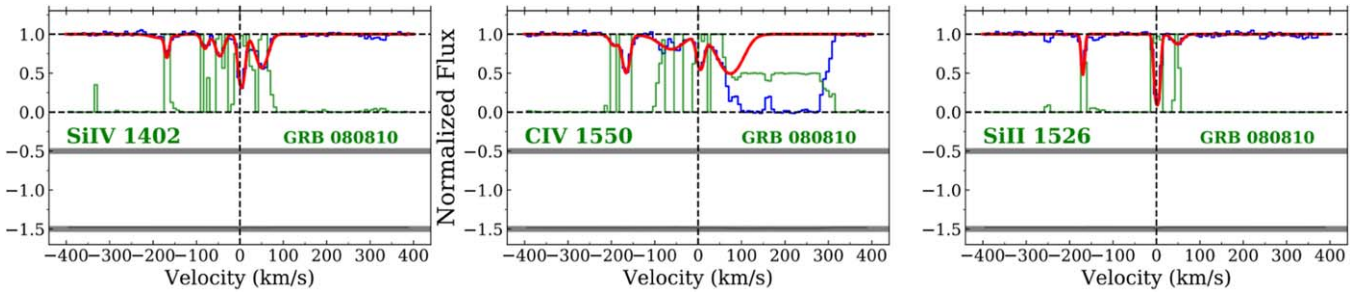


**Figure 13.** Covering fractions calculated for C IV and Si IV doublets, and approximated for Si II 1526 in GRB 080810. The blue, red, and green lines show the normalized flux, Voigt profile fit, and covering fraction, respectively. The error in the flux is shown in the bottom panel, offset by −1.5.

ERC, NOVA, and NWO-M grants; Target; the University of Padova; and the University Federico II (Naples).

*Facilities:* Very Large Telescopes, Lowell Discovery Telescope, Spitzer Space Telescope, Hubble Space Telescope, Neil Gehrels Swift Observatory.

*Software:* `galfit` (Peng et al. 2002), `astropy` (Robitaille et al. 2013), `ESOreflex` (Freudling et al. 2013), `lifelines` (Davidson-Pilon 2019).

## Appendix A
## Covering Fraction

A covering fraction ($C_f$) of 1 was assumed in deriving the Voigt profile fits and column densities used in this paper (Gatkine et al. 2019). Here we present a more quantitative rationale for that assumption. A typical feature of partial covering fraction cases is line saturation with residual positive flux. We do not see that in any of the GRB sightlines in this sample, suggesting a high covering fraction. All the line saturations go to zero flux (see Figures 17–43 in Gatkine et al. 2019).

Second, in Gatkine et al. (2019), all the doublets were fit using a joint Bayesian fitting for the doublets with an assumption of $C_f = 1$, resulting in reasonable fits for both the components of the doublets, which suggest that a $C_f$ of 1 is a consistent assumption. Lastly, the UV-emitting region for a GRB during the first 1–2 days after the GRB explosion (typically the timescale when the spectra are obtained) is extremely tiny (∼1–2 light days ∼100−200 au). This is much more compact than the typical cloud sizes expected for the outflows, which can be estimated as $\frac{\text{total column density}}{\text{density}}$ $\sim 10^{18}/10^{-2}$ cm $\sim 10^{20}$ cm $\gg$ 100–200 au. Here, we take a typical H I column density as the total column density, and $10^{-2}$ cm$^{-3}$ as a typical density for the outflow absorbers. Similarly, Liang & Remming (2020) suggest a cloud diameter of 1–2 pc. Hence, the GRB sightline can be treated as a pencil beam, and therefore a covering fraction of 1 is a reasonable assumption.

Furthermore, we computed the $C_f$ for the C IV and Si IV doublets, and approximated it for the Si II 1526–Si II 1190 pair using the formalism described in Hamann et al. (1997). An example is shown in Figure 13. Note that the ratio of (oscillator strength × $\lambda$) needs to be ∼2 for the formalism in Hamann et al. (1997), and hence the $C_f$ for Si II 1526 is only an approximation. The covering fraction, shown in green, is always $\gtrsim$0.75 for the line components. Therefore, the assumption of $C_f = 1$ is a reasonable assumption for our CGM–GRB sample probed by the GRB sightline.

## Appendix B
## Additional Outflow–Galaxy Correlations

In this appendix section, we discuss the weaker ($<2\sigma$) outflow–galaxy correlations to provide the full scope of correlations investigated for the CGM–GRB sample. Deeper observations of the host galaxies and a larger sample will be required to evaluate these correlations in the future.

### *B.1.* $N_{out}$ *versus* $M_*$

From visual inspection of the $N_{\rm out}$ versus $M_*$ panels in Figure 14, there is a minor rise in $N_{\rm out}$ of high ions with stellar mass (better seen in C IV and Si IV), albeit with weak statistical significance (i.e., a high value of the Kendall-$\tau$ $p$-value). More quantitatively, the correlation exists with confidence levels of 80% and 74% in C IV and Si IV, respectively. The Si IV plot also shows a significantly larger spread in column density at a higher stellar mass. On the other hand, the low ions do not show any difference between the low-mass and high-mass samples (as evident from the CDF plots and high $p$-values). Thus, the overall column density of the low-ion outflow remains independent of the stellar mass, and shows a weak correlation for the column density of the high-ion outflow. This finding implies that the prevalence of low-ion-traced outflows is largely independent of the stellar mass, and for high-ion outflows (particularly Si IV), it is only moderately boosted at high $M_*$. Given the large spread (∼2 dex) in the column densities at any mass (for both high and low ions), it is clear that the relation between outflow column density and stellar mass, if any, is complex, with multiple contributing factors such as halo mass, SFR, and ionization state.

### *B.2.* $N_{out}$ *versus sSFR*

We investigated the correlations, if any, between outflow column density ($N_{\rm out}$) and specific SFR (sSFR = SFR/$M_*$) in Figure 15. We do not see any statistically significant correlation. Previous studies at lower redshifts have shown only a weak or no correlation between outflow column density and sSFR for either low-ion or high-ion outflows. For instance, Du et al. (2016) see only a weak correlation for C IV-traced outflows at $z \sim 1.25$, while Bradshaw et al. (2013) see no correlation for Mg II-traced outflows at $z \sim 0.7$–1.63. Thus, the lack of $N_{\rm out}$–SFR relations for both high- and low-ions at $z \sim 2$–6 in our data is consistent with previous results at lower redshifts.

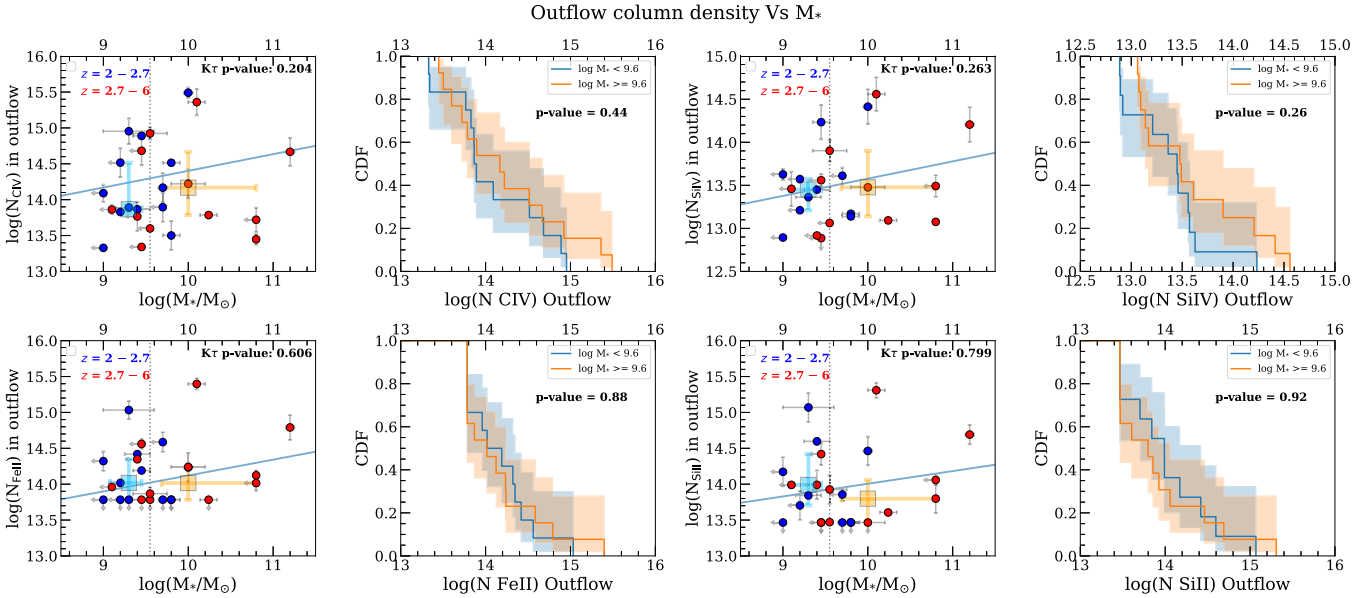


**Figure 14.** The same as Figure 3, for the outflow column density vs. $M_*$.

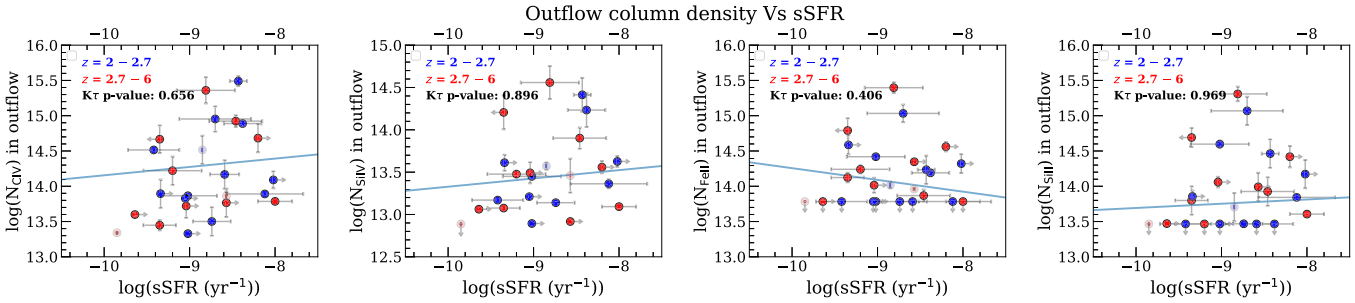


**Figure 15.** The same as Figure 3, for outflow column density vs. specific SFR. The objects where both SFR and $M_*$ are not detected are shown in a lighter shade.

### *B.3. Outflow* $V_{max}$ *versus* $M_*$

This relation is summarized in Figure 16. We observe a weak correlation in C IV (84% confidence or $\sim 1.5\sigma$) and a slightly stronger correlation in Si IV (98% confidence or $\sim 2.5\sigma$). We note a larger spread in the low-$M_*$ group, as evident from the errorbars around the low-$M_*$ group in Figure 16 (top panels). This spread can be directly explained by the larger spread of SFR in the low-$M_*$ group compared to the high-$M_*$ group in Figure 2 (see panel 2). It is the variance in SFR that is directly causing the spread in the $V_{\rm max}$–$M_*$ plot for high ions. By combining this with the result from Appendix B.1, we can deduce that the stellar mass by itself does not significantly affect the kinematics or column density of the high-ion outflows, but is almost entirely driven by the SFR instead.

For low-ion species, we do not see any correlation between $V_{\rm max}$ and $M_*$. We observe a large spread in both high-mass and low-mass groups. Overall, our high-$z$ results for the low-ion-traced outflows show a different picture compared to the results in low-$z$ studies. For instance, Rubin et al. (2014) find a $3.5\sigma$ correlation between $V_{\rm max}$ and $M_*$, and no correlation with current SFR. In contrast, for our sample at $z > 2$, we find a weak correlation ($\sim 2\sigma$ for Si II) with SFR, and no correlation with the stellar mass.

### *B.4. Outflow* $V_{max}$ *versus sSFR*

We summarize the results of the $V_{\rm max}$ versus sSFR correlation in Figure 17. We do not find any statistically significant correlation of sSFR with $V_{\rm max}$. A weak, $1\sigma$ correlation appears to be present for $V_{\rm max}$ versus sSFR for low-ion outflows, albeit with large scatter.

Correlations between outflow kinematics and sSFR have been seen in past observations. For instance, Heckman et al. (2015) and Heckman & Borthakur (2016) report a strong ($>2\sigma$) correlation between outflow velocity of warm ionized gas and sSFR over 2.5 orders of magnitude in sSFR for starburst galaxies at $z < 0.2$. Bradshaw et al. (2013) suggest a $V_{\rm max}$–SFR correlation at $z \sim 0.7$–$1.63$, but this is shallower compared to the $z \sim 0$ correlation. Sugahara et al. (2017) also report $V_{\rm max}$–SFR correlations at $z \sim 0$–$1$, albeit with a significant variation with redshift, and over only one order of magnitude in sSFR. For comparison, we explore this correlation over almost two orders of magnitude in sSFR, and do not find any statistically significant correlation.

This lack of correlation may be for a number of reasons: (1) an intrinsic weakening of the correlation at high redshifts; (2) the presence of a large scatter in the correlation, thus requiring observations over a larger range in sSFR to see the correlation; or (3) the upper and lower limits in sSFR may mask the

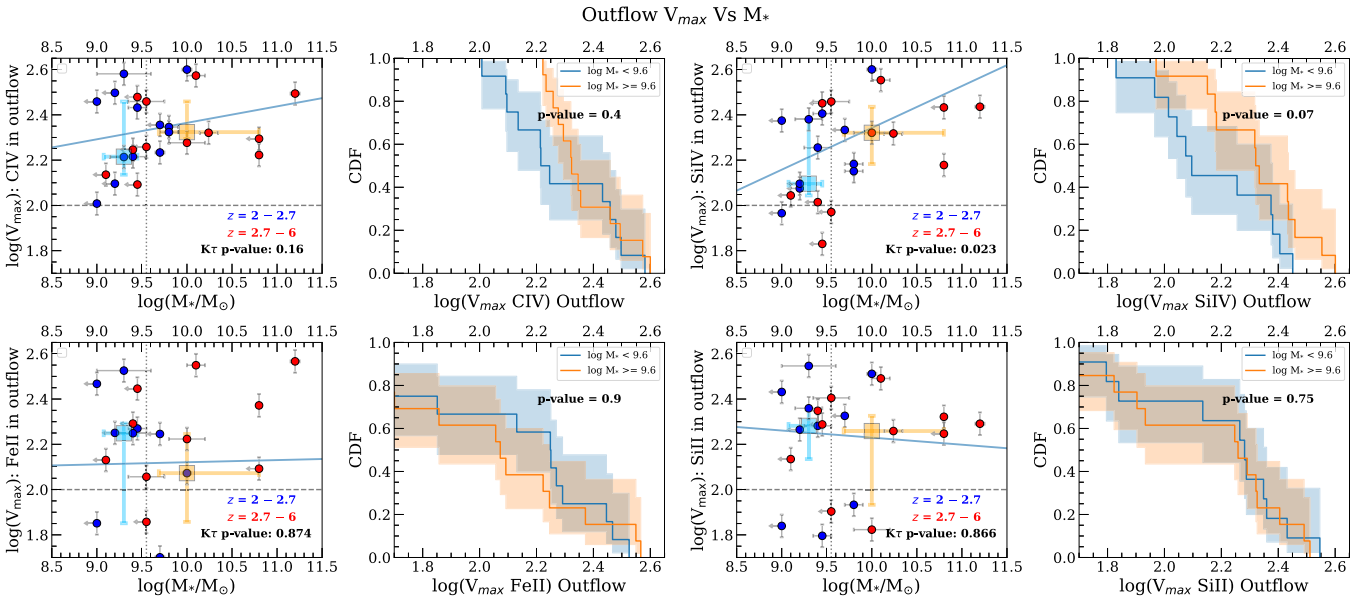


**Figure 16.** The same as Figure 3, for the maximum outflow velocity, $V_{\rm max}$ vs. $M_*$. The horizontal dashed line in the panels shows the 100 km s$^{-1}$ level, which we treat as the threshold for outflow.

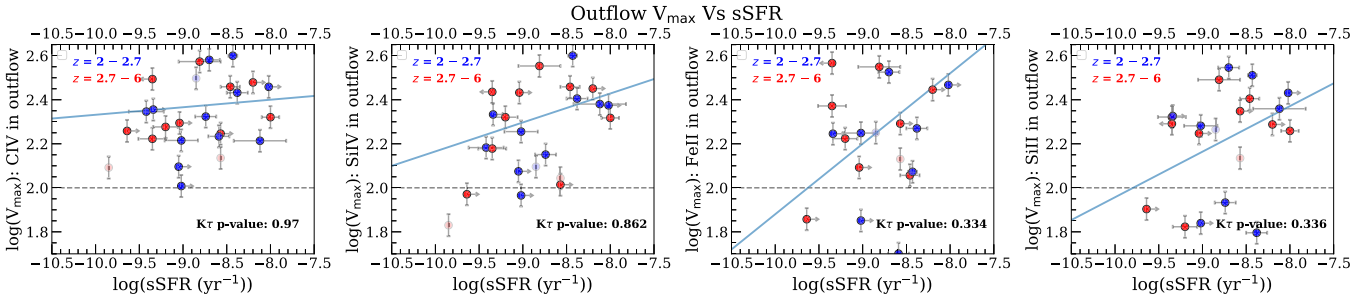


**Figure 17.** The same as Figure 15, for the the scaling relations of the maximum outflow velocity ($V_{\rm max}$) with specific SFR (=SFR/$M_*$). The horizontal dashed line in the panels shows the 100 km s$^{-1}$ level, which we treat as the threshold for outflow.

underlying correlation. In all the three cases, deeper observations of the host galaxy are needed to better constrain the sSFR and, thereby, its relation with the outflow properties.

## Appendix C
## Consideration of Other Low-ion Lines: C II 1334 and O I 1302

As previously explained in Section 3.2, we did not use C II 1334 and O I 1302 for the primary investigation of the outflow–galaxy correlations due to mild concerns about possible blending due to neighboring lines. However, we performed the same analysis for these two lines as a consistency check for the low-ion correlations observed in the main paper. Here we mainly focus on $N_{\rm out}$ and $V_{\rm max}$ versus $M_*$ and SFR. These plots are show in Figures 18 and 19. We observe that the $N_{\rm out,C\ II}$–SFR correlation has a smaller $p$-value ($\sim 2\sigma$) compared to that observed for other low-ion lines. Other than this deviation, we do not see any significant departure in the results compared to those obtained for Si II 1526 and Fe II 1608.

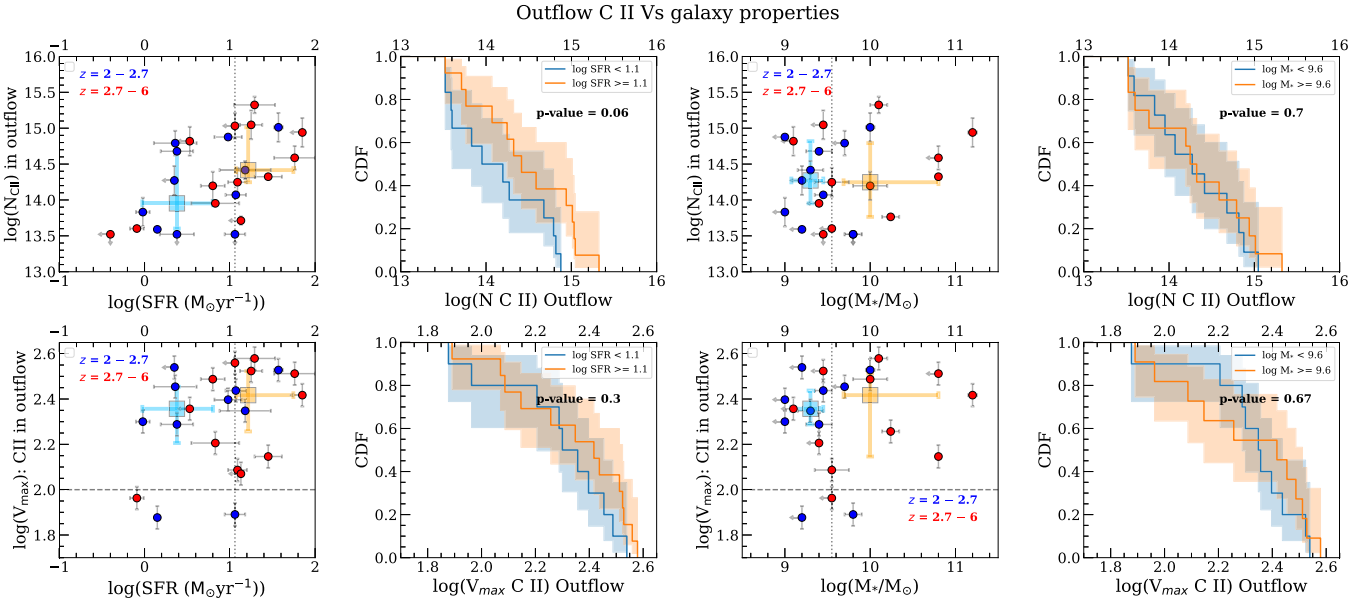


**Figure 18.** The same as Figure 3, for the correlations of the C II 1334-traced outflow with galaxy properties.

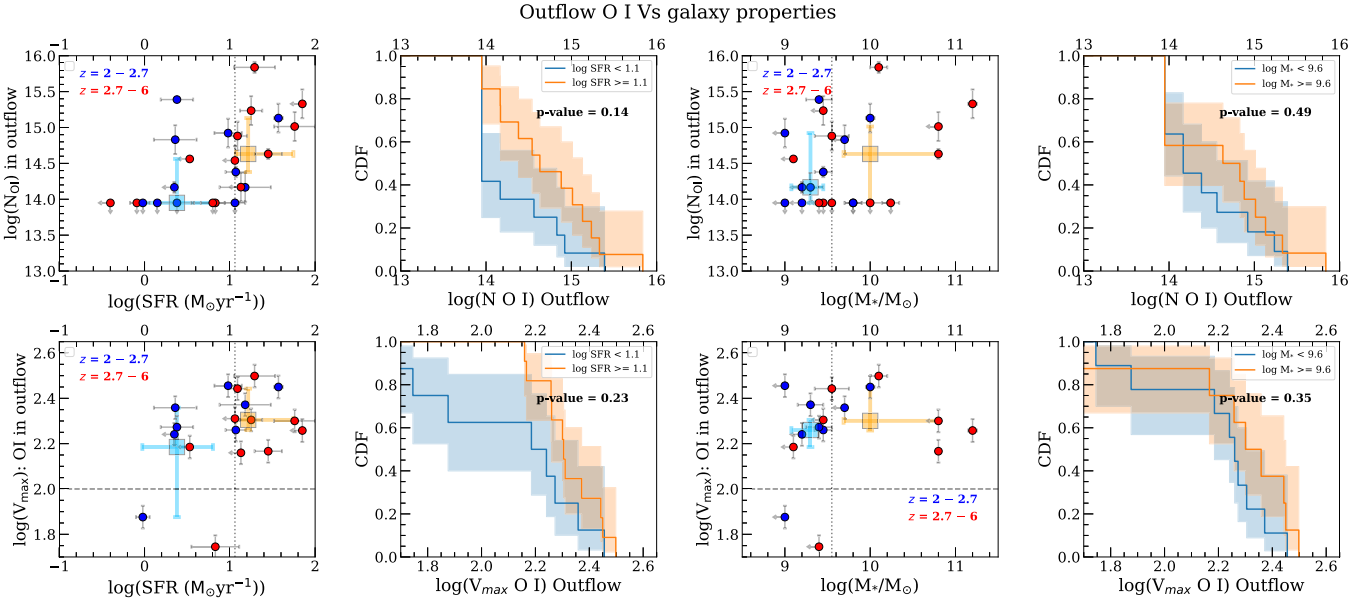


**Figure 19.** The same as Figure 3, for the correlations of the O I 1302-traced outflow with galaxy properties.

## Appendix D
## Relation of O VI Absorption with Galaxy Properties

O VI traces the warm-hot medium ($10^5$–$10^6$ K, assuming collisional equilibrium). It is likely that O VI absorption traces a different phase than the gas traced by C IV and Si IV. Here we look at the same relations studied above with O VI. Due to the location of the O VI doublet in the far-UV ($\lambda_{\rm rest} = 1031.9$ and 1037.6 Å), fewer afterglow spectra in our sample cover the O VI band. Therefore, we caution that the relations observed for O VI are based on a smaller sample than other lines. Regardless, O VI correlations can provide useful insights into the warm-hot phase of the CGM.

From Figure 20, it is clear that both the outflow column density and $V_{\rm max}$ correlate with the stellar mass. The outflow column density is also correlated to the SFR, albeit less so than with the stellar mass. The O VI correlations appear to follow the correlations of high-ion species (C IV and Si IV) described earlier. With a caution of the limited sample size, the data indicates that star formation activity also drives outflows in the O VI-traced phase at $z \sim 2$–6.

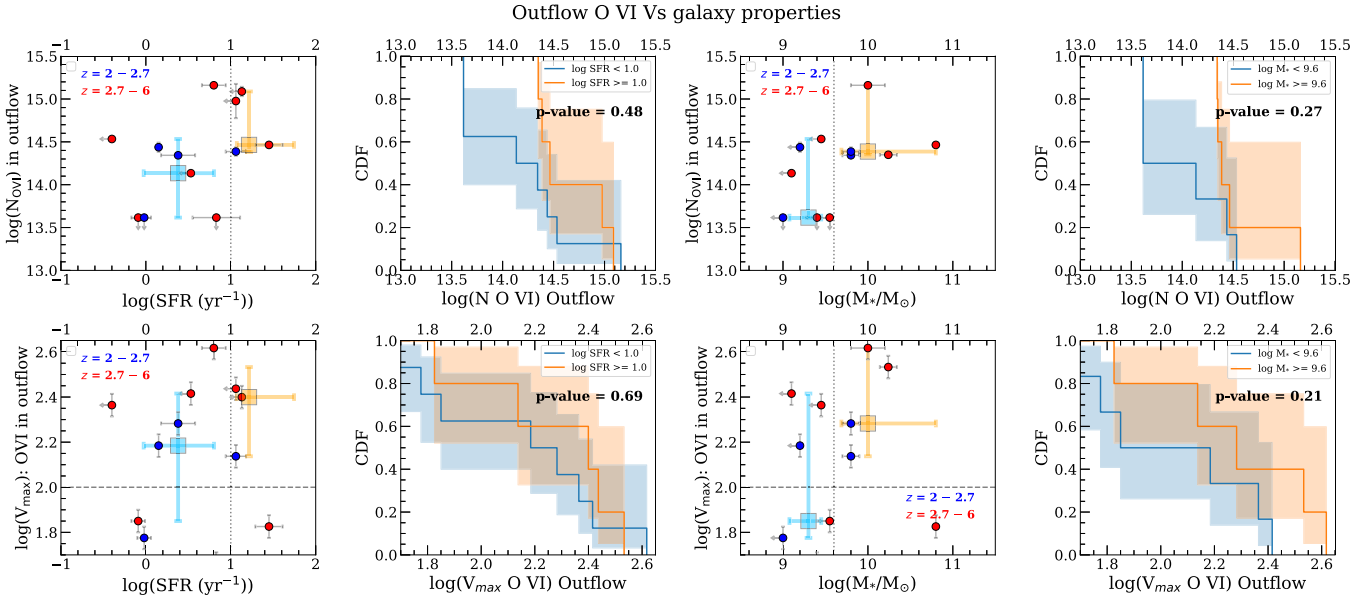


**Figure 20.** The same as Figure 3, for the correlations of the O VI-traced outflow with galaxy properties.

## ORCID iDs

Pradip Gatkine https://orcid.org/0000-0002-1955-2230
Sylvain Veilleux https://orcid.org/0000-0002-3158-6820
Daniel Perley https://orcid.org/0000-0001-8472-1996
Simone Dichiara https://orcid.org/0000-0001-6849-1270
S. Bradley Cenko https://orcid.org/0000-0003-1673-970X
Eleonora Troja https://orcid.org/0000-0002-1869-7817

## References

Alam, S., Albareti, F. D., Prieto, C. A., et al. 2015, ApJS, 219, 12
Beckwith, S. V., Stiavelli, M., Koekemoer, A. M., et al. 2006, AJ, 132, 1729
Benson, A. J. 2010, PhR, 495, 33
Bloom, J. S., Kulkarni, S. R., & Djorgovski, S. G. 2002, AJ, 123, 1111
Bolmer, J., Greiner, J., Krühler, T., et al. 2018, A&A, 609, A62
Booth, C., & Schaye, J. 2013, NatSR, 3, 1738
Bordoloi, R., Lilly, S. J., Hardmeier, E., et al. 2014, ApJ, 794, 130
Bouwens, R., Illingworth, G., Franx, M., et al. 2009, ApJ, 705, 936
Bouwens, R. J., Illingworth, G., Oesch, P., et al. 2014, ApJ, 793, 115
Bradshaw, E., Almaini, O., Hartley, W., et al. 2013, MNRAS, 433, 194
Brown, A., Vallenari, A., Prusti, T., et al. 2018, A&A, 616, A1
Bruzual, G., & Charlot, S. 2003, MNRAS, 344, 1000
Caputi, K., Ilbert, O., Laigle, C., et al. 2015, ApJ, 810, 73
Cardelli, J. A., Clayton, G. C., & Mathis, J. S. 1989, ApJ, 345, 245
Castro, S., Galama, T., Harrison, F., et al. 2003, ApJ, 586, 128
Castro-Tirado, A., Sánchez-Ramírez, R., Ellison, S., et al. 2013, arXiv:1312.5631
Chabrier, G. 2003, PASP, 115, 763
Chen, H.-W., Perley, D. A., Pollack, L. K., et al. 2009, ApJ, 691, 152
Chevalier, R., & Clegg, A. 1985, Natur, 317, 44
Chisholm, J., Tremonti, C. A., Leitherer, C., et al. 2015, ApJ, 811, 149
Chisholm, J., Tremonti, C. A., Leitherer, C., & Chen, Y. 2017, MNRAS, 469, 4831
Chisholm, J., Tremonti, C. A., Leitherer, C., Chen, Y., & Wofford, A. 2016, MNRAS, 457, 3133
Christensen, C. R., Davé, R., Governato, F., et al. 2016, ApJ, 824, 57
Covino, S., Melandri, A., Salvaterra, R., et al. 2013, MNRAS, 432, 1231
Cucchiara, A., Fumagalli, M., Rafelski, M., et al. 2015, ApJ, 804, 51
Davidson-Pilon, C. 2019, JOSS, 4, 1317
de Ugarte Postigo, A., Thöne, C. C., Bolmer, J., et al. 2018, A&A, 620, A119
D'Elia, V., Fiore, F., Meurs, E., et al. 2007, A&A, 467, 629
D'Elia, V., Fynbo, J. P. U., Covino, S., et al. 2010, A&A, 523, A36
D'elia, V., Fynbo, J. P. U., Goldoni, P., et al. 2014, A&A, 564, A38
Du, X., Shapley, A. E., Martin, C. L., & Coil, A. L. 2016, ApJ, 829, 64
Du, X., Shapley, A. E., Reddy, N. A., et al. 2018, ApJ, 860, 75
Erb, D. K., Quider, A. M., Henry, A. L., & Martin, C. L. 2012, ApJ, 759, 26
Evans, D., Riello, M., De Angeli, F., et al. 2018, A&A, 616, A4
Fabian, A. 2012, ARA&A, 50, 455
Feigelson, E., & Nelson, P. 1985, ApJ, 293, 192
Fiore, F., d'Elia, V., Lazzati, D., et al. 2005, ApJ, 624, 853
Flewelling, H., Magnier, E., Chambers, K., et al. 2020, ApJS, 251, 7
Fox, A. J., Ledoux, C., Vreeswijk, P. M., Smette, A., & Jaunsen, A. O. 2008, A&A, 491, 189
Freudling, W., Romaniello, M., Bramich, D., et al. 2013, A&A, 559, A96
Friis, M., De Cia, A., Krühler, T., et al. 2015, MNRAS, 451, 167
Fruchter, A., Levan, A., Strolger, L., et al. 2006, Natur, 441, 463
Frye, B., Broadhurst, T., & Benítez, N. 2002, ApJ, 568, 558
Fynbo, J., Gorosabel, J., Dall, T., et al. 2001, A&A, 373, 796
Fynbo, J., Gorosabel, J., Smette, A., et al. 2005, ApJ, 633, 317
Fynbo, J. P. U., Jakobsson, P., Prochaska, J., et al. 2009, ApJS, 185, 526
Gatkine, P., Veilleux, S., & Cucchiara, A. 2019, ApJ, 884, 66
Gatkine, P., Vogel, S., & Veilleux, S. 2020, ApJ, 897, 9
Gordon, K. D., Clayton, G. C., Misselt, K., Landolt, A. U., & Wolff, M. J. 2003, ApJ, 594, 279
Greiner, J., Bolmer, J., Wieringa, M., et al. 2018, A&A, 614, A29
Greiner, J., Fox, D. B., Schady, P., et al. 2015, ApJ, 809, 76
Hafen, Z., Faucher-Giguère, C.-A., Anglés-Alcázar, D., et al. 2019, MNRAS, 488, 1248
Hamann, F., Barlow, T., Cohen, R., Junkkarinen, V., & Burbidge, E. M. 1997, in ASP Conf. Ser. 128, Mass Ejection from Active Galactic Nuclei, ed. N. Aravm, I. Shlosman, & R. J. Weymann (San Francisco, CA: ASP), 19
Harrison, C., Alexander, D., Swinbank, A., et al. 2012, MNRAS, 426, 1073
Hartoog, O., Malesani, D., Fynbo, J., et al. 2015, A&A, 580, A139
Heckman, T., Borthakur, S., Wild, V., Schiminovich, D., & Bordoloi, R. 2017, ApJ, 846, 151
Heckman, T. M., Alexandroff, R. M., Borthakur, S., Overzier, R., & Leitherer, C. 2015, ApJ, 809, 147
Heckman, T. M., & Best, P. N. 2014, ARA&A, 52, 589
Heckman, T. M., & Borthakur, S. 2016, ApJ, 822, 9
Heintz, K., Bolmer, J., Ledoux, C., et al. 2019, A&A, 629, A131
Heintz, K., Watson, D., Jakobsson, P., et al. 2018, MNRAS, 479, 3456
Henden, A., & Levine, S. 2002, GCN Circ., 1592, https://gcn.gsfc.nasa.gov/gcn/gcn3/1592.gcn3
Hennawi, J. F., Prochaska, J. X., Burles, S., et al. 2006, ApJ, 651, 61
Hirschmann, M., Naab, T., Davé, R., et al. 2013, MNRAS, 436, 2929
Isobe, T., & Feigelson, E. 1990, BAAS, 22, 917
Isobe, T., Feigelson, E., & Nelson, P. I. 1986, ApJ, 306, 490
Kajisawa, M., Ichikawa, T., Tanaka, I., et al. 2009, ApJ, 702, 1393
King, A., & Pounds, K. 2015, ARA&A, 53, 115
Krühler, T., Greiner, J., McBreen, S., et al. 2009, ApJ, 697, 758
Krühler, T., Greiner, J., Schady, P., et al. 2011, A&A, 534, A108
Krühler, T., Malesani, D., Fynbo, J., et al. 2015, A&A, 581, A125
Kuijken, K., Heymans, C., Dvornik, A., et al. 2019, A&A, 625, A2
Lehner, N., O'Meara, J. M., Fox, A. J., et al. 2014, ApJ, 788, 119

Li, L., Wang, Y., Shao, L., et al. 2018, ApJS, 234, 26
Liang, C. J., & Remming, I. 2020, MNRAS, 491, 5056
Littlejohns, O., Butler, N., Cucchiara, A., et al. 2015, MNRAS, 449, 2919
Littlejohns, O., Willingale, R., O'brien, P., et al. 2012, MNRAS, 421, 2692
Lodders, K. 2003, ApJ, 591, 1220
Lyman, J., Levan, A., Tanvir, N., et al. 2017, MNRAS, 467, 1795
Martin, C. L., & Bouché, N. 2009, ApJ, 703, 1394
Massey, P., Dunham, E., Bida, T., et al. 2013, AAS Meeting, 221, 345.02
McCauley, L., & Melandri, A. 2015, GCN Circ., 18432, https://gcn.gsfc.nasa.gov/gcn3/18432.gcn3
Meurer, G. R., Heckman, T. M., & Calzetti, D. 1999, ApJ, 521, 64
Milvang-Jensen, B., Fynbo, J. P., Malesani, D., et al. 2012, ApJ, 756, 25
Mitchell, P. D., Schaye, J., Bower, R. G., & Crain, R. A. 2020, MNRAS, 494, 3971
Mo, H., & White, S. 2002, MNRAS, 336, 112
Muratov, A. L., Kereš, D., Faucher-Giguère, C.-A., et al. 2015, MNRAS, 454, 2691
Murray, N., Quataert, E., & Thompson, T. A. 2005, ApJ, 618, 569
Nelson, D., Pillepich, A., Springel, V., et al. 2019, MNRAS, 490, 3234
Nielsen, N. M., Kacprzak, G. G., Pointon, S. K., et al. 2020, ApJ, 904, 164
Page, K. L., Willingale, R., Bissaldi, E., et al. 2009, MNRAS, 400, 134
Peng, C. Y., Ho, L. C., Impey, C. D., & Rix, H.-W. 2002, AJ, 124, 266
Perley, D., Tanvir, N. R., Hjorth, J., et al. 2016, ApJ, 817, 8
Perley, D. A., Cenko, S., Bloom, J., et al. 2009, AJ, 138, 1690
Pizzati, E., Ferrara, A., Pallottini, A., et al. 2020, MNRAS, 495, 160
Prochaska, J., Chen, H.-W., Bloom, J., et al. 2007, ApJS, 168, 231
Prochaska, J. X., Dessauges-Zavadsky, M., Ramirez-Ruiz, E., & Chen, H.-W. 2008, ApJ, 685, 344
Prochaska, J. X., Lau, M. W., & Hennawi, J. F. 2014, ApJ, 796, 140
Rigby, J., Bayliss, M., Sharon, K., et al. 2018, AJ, 155, 104
Robitaille, T. P., Tollerud, E. J., Greenfield, P., et al. 2013, A&A, 558, A33
Rubin, K. H., Prochaska, J. X., Koo, D. C., & Phillips, A. C. 2012, ApJL, 747, L26
Rubin, K. H., Prochaska, J. X., Koo, D. C., et al. 2014, ApJ, 794, 156
Rudie, G. C., Steidel, C. C., Pettini, M., et al. 2019, ApJ, 885, 61
Rupke, D. S. 2018, Galax, 6, 138
Savage, B. D., & Sembach, K. R. 1991, ApJ, 379, 245
Savaglio, S., Glazebrook, K., & Le Borgne, D. 2009, ApJ, 691, 182
Schady, P., Dwelly, T., Page, M. J., et al. 2012, A&A, 537, A15
Schaye, J., Carswell, R. F., & Kim, T.-S. 2007, MNRAS, 379, 1169
Schlafly, E. F., & Finkbeiner, D. P. 2011, ApJ, 737, 103
Schmitt, J. 1985, ApJ, 293, 178
Selsing, J., Malesani, D., Goldoni, P., et al. 2019, A&A, 623, A92
Shapley, A. E., Steidel, C. C., Pettini, M., & Adelberger, K. L. 2003, ApJ, 588, 65
Sharma, M., & Nath, B. B. 2012, ApJ, 763, 17
Shen, S., Madau, P., Guedes, J., et al. 2013, ApJ, 765, 89
Smette, A., Ledoux, C., Vreeswijk, P., et al. 2013, GCN Circ., 14848, https://gcn.gsfc.nasa.gov/gcn3/14848.gcn3
Sparre, M., Hartoog, O., Krühler, T., et al. 2014, ApJ, 785, 150
Speagle, J. S., Steinhardt, C. L., Capak, P. L., & Silverman, J. D. 2014, ApJS, 214, 15
Steidel, C. C., Erb, D. K., Shapley, A. E., et al. 2010, ApJ, 717, 289
Sugahara, Y., Ouchi, M., Harikane, Y., et al. 2019, ApJ, 886, 29
Sugahara, Y., Ouchi, M., Lin, L., et al. 2017, ApJ, 850, 51
Swinbank, A., Vernet, J., Smail, I., et al. 2015, MNRAS, 449, 1298
Thöne, C., Fynbo, J. P. U., Goldoni, P., et al. 2012, MNRAS, 428, 3590
Toy, V. L., Cucchiara, A., Veilleux, S., et al. 2016, ApJ, 832, 175
Tumlinson, J., Peeples, M. S., & Werk, J. K. 2017, ARA&A, 55, 389
Turner, M. L., Schaye, J., Steidel, C. C., Rudie, G. C., & Strom, A. L. 2014, MNRAS, 445, 794
Veilleux, S., Cecil, G., & Bland-Hawthorn, J. 2005, ARA&A, 43, 769
Veilleux, S., Maiolino, R., Bolatto, A. D., et al. 2020, A&ARv, 28, 2
Wechsler, R. H., & Tinker, J. L. 2018, ARA&A, 56, 435
Weiner, B. J., Coil, A. L., Prochaska, J. X., et al. 2009, ApJ, 692, 187
Wiseman, P., Schady, P., Bolmer, J., et al. 2017, A&A, 599, A24
Xu, D., Vreeswijk, P., Fynbo, J., et al. 2014, GCN Circ., 17040, https://gcn.gsfc.nasa.gov/gcn3/17040.gcn3
Zafar, T., Møller, P., Watson, D., et al. 2018, MNRAS, 480, 108